Geothermal reservoir rocks of the Büyük Menderes Graben (Turkey): stratigraphic correlation by a multiproxy approach

Dorothee SIEFERT[1,2,]*, Markus WOLFGRAMM[3], Thomas KÖLBEL[2],
Johannes GLODNY[4], Jochen KOLB[1], Elisabeth EICHE[1]

[1]Chair of Geochemistry and Economic Geology, Institute of Applied Geosciences, Karlsruhe Institute of Technology, Karlsruhe, Germany
[2]EnBW Energie Baden-Württemberg AG, Karlsruhe, Germany
[3]Geothermie Neubrandenburg GmbH, Neubrandenburg, Germany
[4]GFZ German Research Centre for Geosciences, Potsdam, Germany

Abstract: This paper focuses on the correlation of two different marble units from an approximately 3,900 m deep geothermal exploration well (GP-1) in western Turkey by petrographical and geochemical data. Future geothermal exploration drilling in that area will benefit from a better (tectono) stratigraphic correlation and a better definition of the reservoir geometry in the basin. It is an innovative approximation in many settings to correctly correlate marble units without clear stratigraphic markers or fossil record, in particular, when sample material is restricted to cuttings. The most distinctive petrographical and geochemical properties in this study are colour, light transmission along with rare-earth element + yttrium (REY) geochemistry, and stable carbon and oxygen isotope data. Two stratigraphic correlations can be maintained for two different marble horizons of the GP-1 well to different stratigraphic horizons outcropping in the study area. Additional Rb-Sr geochronology yields an age of the last metamorphic overprint of the marbles of approximately 30 Ma. This study shows that a multiproxy approach is required to yield a reliable stratigraphic correlation as an important component of geothermal exploration, which supports the conceptual geological model prior to further geothermal drilling.

Key words: Marble, multiproxy approach, carbon and oxygen stable isotopes, REY, Rb-Sr geochronology, Menderes Massif

1. Introduction

Geothermal power production experienced a rapid development in Turkey in recent years with an installed electrical capacity of more than 1.5 GW$_{el}$ so far (Murdock et al., 2021). The vast majority of the geothermal power plants are in the Büyük Menderes and Gediz Graben of the Menderes Massif in Western Turkey (Figure 1).

The geological evolution of the Menderes Massif, starting in Neoproterozoic times, led to a complex geological architecture and a rich inventory of deformation structures. Detailed descriptions of the development of the Menderes Massif can be found in Bozkurt (2000), Bozkurt and Oberhänsli (2001) and Gessner et al. (2013). Since the Miocene, crustal thinning resulted in the formation of east-west trending, extensional graben structures (Figure 1; Bozkurt and Oberhänsli, 2001; Gessner et al., 2001a; Régnier et al., 2003; Reilinger et al., 2006). The basement rocks of the graben – consisting of metamorphic and igneous rocks – are overlain by sediments and sedimentary rocks with a thickness of several hundred metres (Figures 1 and 2; Gürer et al., 2009).

With a few exceptions, the geothermal reservoirs in the graben are located in schist and marble units and schist-marble intercalations (Şimşek, 1985). As marble may represent efficient geothermal reservoirs, the understanding of the local geological setting is key for expansion of existing geothermal sites and the overall development of geothermal power production from a regional perspective. Outcrops of these units are accessible at the southern and northern escarpments and were examined in detail in the past. Two different marble-bearing horizons are distinguishable within the area around the Büyük Menderes Graben: one of Paleozoic and another of Mesozoic (Cretaceous) age (Figure 2; Ring et al., 1999; Gessner et al., 2001a; Özer and Sözbilir, 2003).

The composition of marble in general is controlled by (1) the composition of the precursor limestone, (2) metamorphism, (3) fluid-rock interaction, and (4) weathering (Gorgoni et al., 1998). Characterization of marble is usually based on multiproxy approaches, covering different rock properties (Germann et al., 1980; Herz, 1987; Gorgoni et al., 1998; Cramer, 2004; Origlia et

* Correspondence: dorothee.siefert@partner.kit.edu
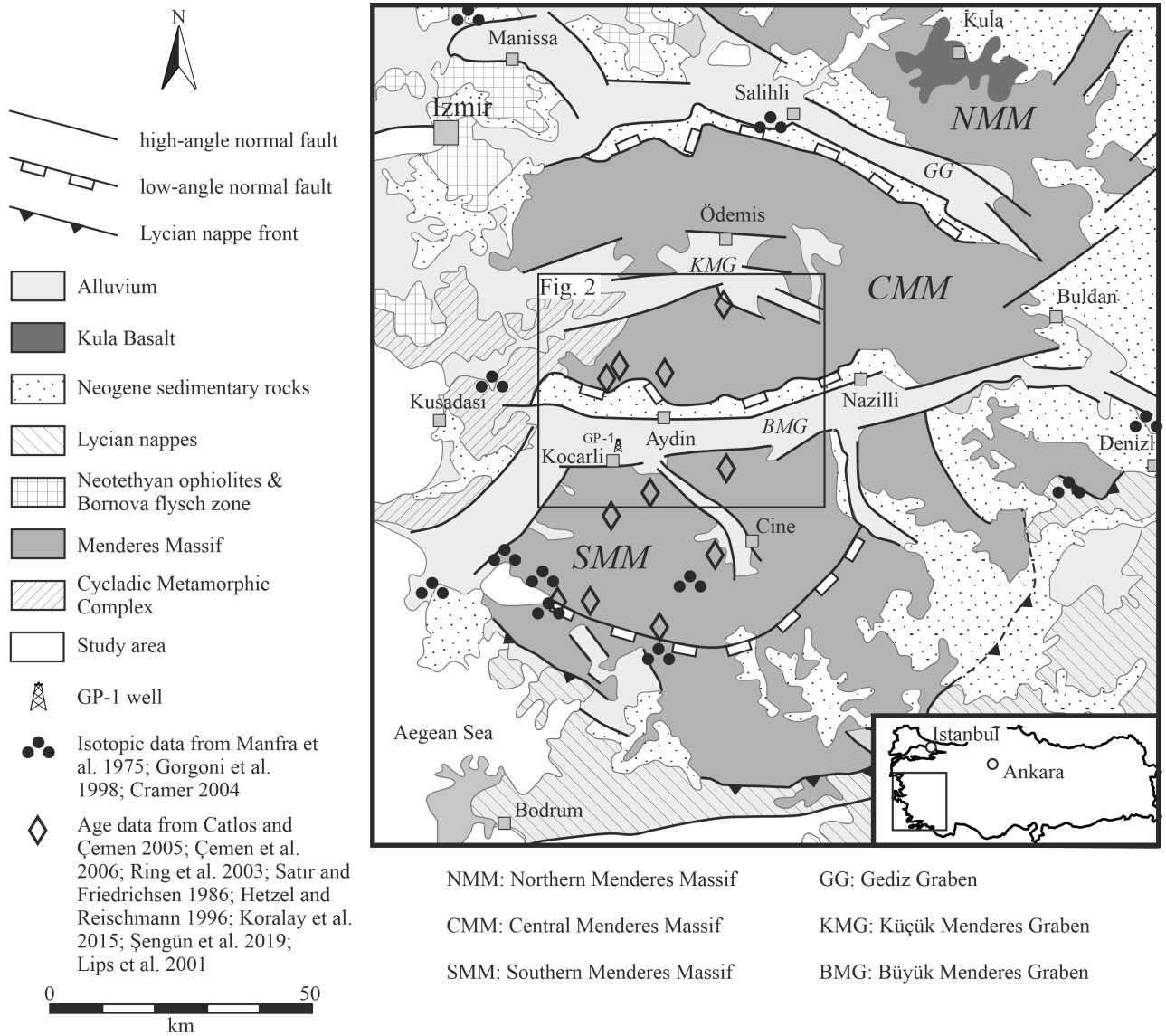
Figure 1. Simplified geological map of the Menderes Massif with the location of the study area (Figure 2) (modified after Kaya, 2015). The central graben is the Büyük Menderes Graben (BMG). Marble outcrops studied by Manfra et al. (1975), Gorgoni et al. (1998) and Cramer (2004) are used for comparison. Locations with available geochronological data are shown.

al., 2012; Ricca et al., 2015). Besides macroscopic features like mineral assemblage and colour, the maximum grain size of specific minerals can be a useful tool (e.g. Ricca et al., 2015). Furthermore, major, trace and rare-earth element (REE) data (e.g. Cramer, 2004) as well as C and O isotope data (e.g. Manfra et al., 1975; Germann et al., 1980) and Rb-Sr geochronology (e.g. Satır and Friedrichsen, 1986) are important features for characterization. Spry (1969) sets a petrographical characterization of metamorphic rocks by analysing both texture and mineral assemblage as essential to an understanding of the rocks. In addition to the mineral assemblage and the purity of a marble (Rosen et al., 2007), the appearance as well as the maximum grain

size and the distribution of the carbonate minerals (calcite and dolomite) can be supportive when characterizing a marble (Germann et al., 1980; Cramer, 2004; Ricca et al., 2015).

Several geochemical analytical methods were applied for provenance analysis of marbles (e.g. Germann et al., 1980) including mass spectrometry for determination of major and trace elements (e.g. Germann et al., 1980; Cramer, 2004; Ricca et al., 2015). Existing positive or negative anomalies of REE and yttrium (REY) can be supportive when investigating redox conditions and evaluating freshwater or seawater origin. Cerium (Ce) anomaly variations are a function of variable redox
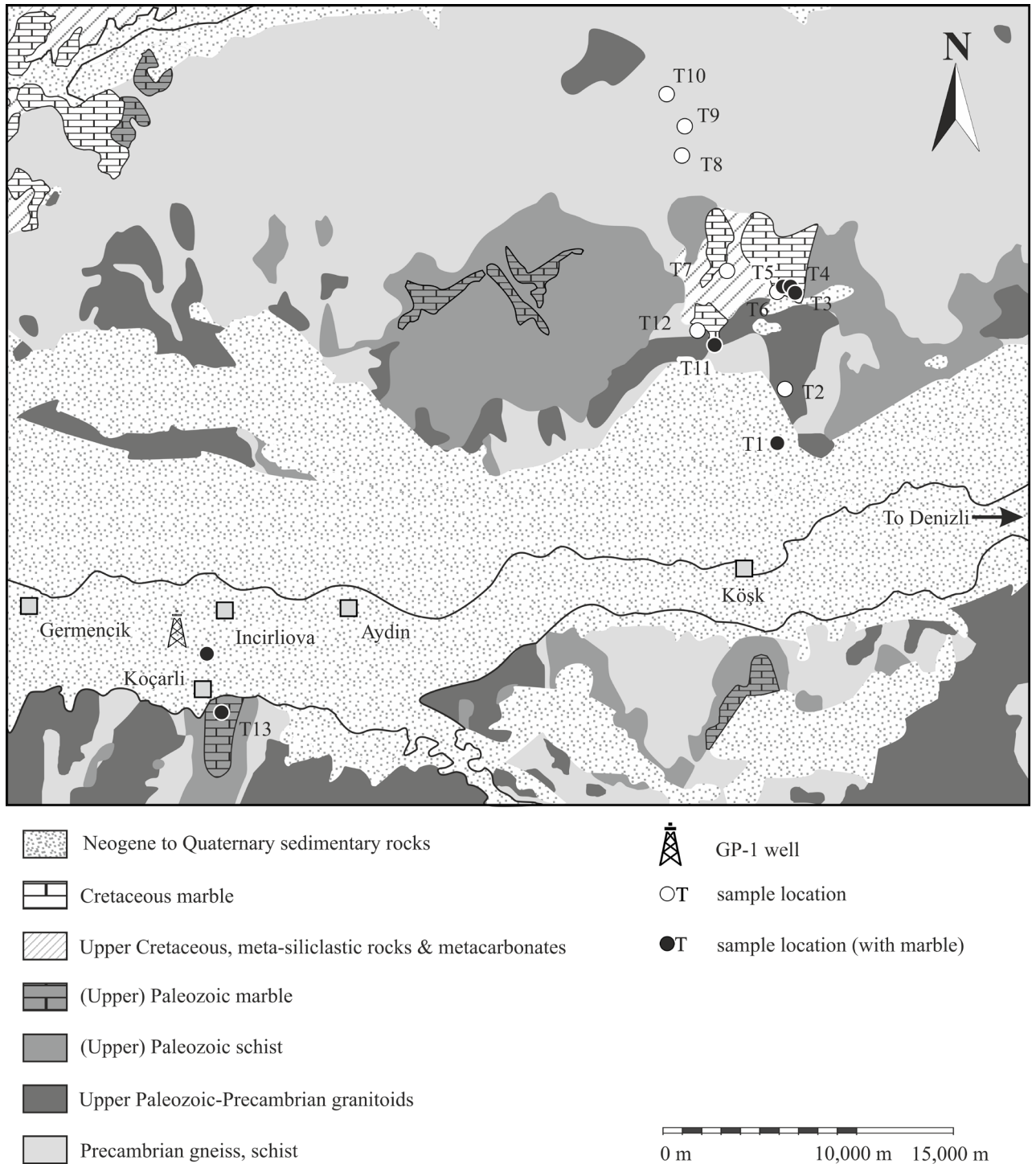
Figure 2. Geological map of the study area with borehole GP-1 and outcrop locations (modified after General Directorate of Mineral Research and Exploration, Turkey, 2015).

potentials (Bau and Dulski, 1996), which are found in natural sedimentary environments. A negative Ce anomaly is indicative of oxic conditions in seawater (Bau and Dulski, 1996; Hua et al., 2013; Tostevin et al., 2016).

Positive anomalies of Y can be classified as large (Y/Ho = 40-80), representing open marine settings, and small (Y/Ho = 33-40), being indicative of near shore settings (Tostevin et al., 2016). In addition, Webb and Kamber

(2000) give a threshold for a Y/Ho mass ratio of ≥ 44, which indicates a strong seawater influence. Positive Eu anomalies with values around 1.5 (Tostevin et al., 2016) can be observed when the seawater signal is overprinted by hydrothermal fluids (Meyer et al., 2012). Rubidium/ strontium (Rb/Sr) geochronology may provide insights into the rock's age and metamorphic evolution (Satır and Friedrichsen, 1986).

Globally, marble $\delta^{13}C_{VPDB}$ values range from –5 to +5 ‰ and $\delta^{18}O_{VSMOW}$ from 18 to 34 ‰ (Rollinson, 1993). The primary isotopic signature acquired during limestone deposition and subsequent secondary processes, such as recrystallisation during metamorphism or fluid-rock interaction, lead to a characteristic isotopic fingerprint of different marble units. Therefore, C and O isotopes are commonly used to determine the marble origin (e.g. Craig and Craig, 1972; Manfra et al., 1975; Herz, 1987). Herz and Dean (1986) found that homogeneous isotopic composition in marbles can be perceived at a broad scale. However, in order to encounter a homogenous isotopic composition within a marble unit, the deposition and subsequent diagenesis of the limestone should occur under uniform physicochemical conditions and isotopic equilibrium must be attained and preserved during metamorphism (Herz and Dean, 1986). Furthermore, it is necessary that the marble unit is chemically homogeneous, has a significant thickness and underwent only a gentle metamorphic gradient (Herz and Dean, 1986).

During an exploration campaign in the vicinity of the Koçarli village, Büyük Menderes Graben (BMG), an approximately 3,900 m deep well (GP-1) was drilled in 2017 (Figure 2). The GP-1 well intersects two marble units at shallow depth and at bottom hole, separated by different metamorphic and igneous rocks of more than 2000 m thickness. Cuttings from the two marble units have been examined along with marble samples from outcrops collected from the northern and southern escarpments of the BMG. Our multiproxy approach characterizes these marbles by their petrographical and geochemical features and their C and O isotope signatures. Furthermore, Rb-Sr geochronology is used to detect potentially contrasting metamorphic ages and initial Sr-isotopic ratios.

The aim of this publication is to demonstrate that surface analogues can be used to stratigraphically classify drilled intersections using a suitable multiproxy approach. This methodology can also be applied to other locations related to graben systems. We compare cutting samples with different, stratigraphically well-defined marble samples from surface outcrops. We manage to allocate the two marble horizons of the cutting samples to the stratigraphically well-defined surface outcrops of marble of different age (Cretaceous and Paleozoic).

2. Regional geology

The Menderes Massif in western Anatolia consists of Proterozoic to Mesozoic, greenschist to amphibolite facies metamorphic rocks (Figure 1; cf. Bozkurt and Oberhänsli, 2001). They are mainly augengneiss, meta-granite, schist, marble, paragneiss and meta-gabbro (Satır and Friedrichsen, 1986; Gürer et al., 2009). Structural upper sections of this basal gneiss unit show an intercalation of quartzite and schist (Şimşek, 1985). This unit is overlain by the so-called mica schist unit. The stratigraphically uppermost unit of the metamorphic rocks is an intercalation of marble, calcareous schist, quartzite, and schist that is significantly fractured (Iğdecik Formation, Şimşek, 1985). The marbles are most likely of marine origin based on structural and tectonic observations, marine fossil findings and isotopic data (Şengör and Yilmaz, 1981; Özer and Sözbilir, 2003; Cramer, 2004).

The Neogene sedimentary cover (Figure 1) consists of breccia, conglomerate, sandstone, clay stone, marl and in places coal seams, mainly deposited in shallow water environment (Gürer et al., 2009; Şimşek, 1985). This Lower Pliocene formation (Kızılburun Formation) represents the earliest continental to lacustrine deposit above the Menderes Massif metamorphic rocks (Şimşek, 1985). On the Kızılburun Formation, there are yellowish to light brown sandstone, clay stone and clayey limestone (Kolankaya Formation, locally Sazak Formation). Fossil-bearing, clayey limestone, sandstone, clay stone and a poorly solidified conglomerate originate from the Pliocene to Quaternary (Tosunlar Formation). Alluvial sediments are represented by terrace deposits, travertine, alluvial debris fans and slope debris (Şimşek, 1985).

During the Alpine orogeny, the tectonic units of the Adriatic Plate and the continental fragments were stacked simultaneously to the subduction of the Neotethys. The evolution of the Menderes Massif is still a matter of debate. Either a "core-cover model" (Dürr et al., 1978; Bozkurt and Oberhänsli, 2001; Rimmelé, 2003; Rimmelé et al., 2003; Bozkurt, 2007; Candan et al., 2011) or a "nappe stacking model" (Dixon and Robertson, 1984; Ring et al., 2001; Gessner et al., 2001b; Gessner et al., 2002; Ring et al., 2003; Régnier et al., 2003; Erdoğan and Güngör, 2004; Gessner et al., 2013) are postulated. The "core-cover model" is based on large-scale correlation between Aegean and Anatolian units. Therefore, the model assumption is to parallelize units from the Greek Islands with units mapped in western Anatolia, Turkey. It separates the meta-sedimentary rocks and the metamorphic schist and gneiss into cover and core series. The contact between the core and the cover is either interpreted as a major unconformity (e.g. Schuiling, 1962) or as essentially intrusive reactivated as a major shear zone (e.g. Bozkurt and Park, 1994). The augengneiss, meta-granite and schist are allocated to the core facies, while the meta-sedimentary rocks (marble, paragneiss) represent

an envelope-like cover (Supplementary Material 1). Both units are assumed to be separated by a large fault system (Rimmelé et al., 2003; Bozkurt and Oberhänsli, 2001).

In the "nappe stacking model", the nappes are named Bayındır, Bozdağ, Çine and Selimiye nappes from bottom to top (e.g. Figure 2 of van Hinsbergen et al., 2010). The Bayındır nappe consists predominantly of phyllite, quartzite, marble and greenschist, indicating a lower metamorphic grade compared to the other nappes. Alpine greenschist facies metamorphism is dated by Ar-Ar on white mica at > 37 Ma (Lips et al., 2001). The Bozdağ nappe comprises mainly meta-pelite and meta-granite with some eclogite and amphibolite intercalations. The protolith age remains unknown. Gessner et al. (1998) suggest a Precambrian age based on the analysis of structural data. The age determination of the granitic rocks by $^{207}Pb/^{206}Pb$ zircon dating indicates an intrusion age of 230–240 Ma (Ring et al., 2001). The Çine nappe consists mainly of orthogneiss, meta-granite and pelitic gneiss accompanied by eclogite and amphibolite lenses. The intrusion age of the orthogneiss protolith is dated at 560–540 Ma (U-Pb zircon age), with decreasing age from south to north (Ring et al., 2001). The age of the meta-granite protolith is determined at 530–540 Ma (U-Pb zircon age, Ring et al., 2001). The Selimiye nappe is subdivided into (1) the lower section consisting of meta-pelite and weakly-deformed meta-granite and (2) the upper part composed of meta-pelite, meta-basite and marble. Uranium-Pb zircon ages of the meta-granite of the lower nappe section yield ca. 549 Ma indicating a Precambrian protolith age of the meta-pelite (Ring et al., 2001). An age from Devonian to Carboniferous is estimated for the upper nappe section supported by fossils (Schuiling, 1962; Cağlayan et al., 1980; Régnier et al., 2003; Supplementary Material 1).

The Menderes Massif is crosscut by three roughly East-West striking graben systems into three submassifs (Figure 1). The Neogene BMG has a width of 8 to 12 km and a length of approximately 125 km. It separates the central and the southern Menderes Massif (CMM and SMM, Bozkurt, 2000). Bozkurt and Oberhänsli (2001) describe the graben systems as a result of "basin-and-range"-like extension of Neogene age. In the graben system, the geological units are divided into different compartments by antithetic faults.

3. Study area

The BMG graben filling consists of Neogene to Quaternary sedimentary rocks, whereas the graben shoulder comprises the metamorphic sequence of the Menderes Massif as described above. In the northern part, a Cretaceous marble is present along with a Paleozoic marble horizon and meta-carbonate rocks. Further north, a large area is covered by a Precambrian gneiss and schist sequence. The analogue stratigraphy is presented in the southern part of the rift system; however, the outcrops of the Cretaceous part are lacking.

Geothermal power generation in the BMG has a long history starting with a pilot power plant constructed at the Kızıldere geothermal field close to Denizli in 1975 followed by the first commercial power plant in the same field with an electrical gross capacity of 15 MW (Aksoy, 2014). Additional plants in western Turkey that are located within the BMG increased the total capacity to 311 MW in 2013 (Aksoy, 2014). Most of the (more than 10) existing power plants in the BMG, a majority located at the northern escarpment in Aydın and Denizli, have an intercalation of marble, schist, and gneiss as reservoir rock. The marble horizons are described as the reason for the relatively high CO_2-contents of the produced geothermal fluid with an approximate average of 2.5 wt-% CO_2 (Aksoy, 2014).

4. Methods

4.1. General procedure and petrography

In total, 17 marble surface and cutting samples were analysed by different methods (Supplementary Material 2). The study area is located in the BMG (Figure 1) including its northern and southern escarpment. The location of the 3,900 m deep geothermal exploration well GP-1 and the outcrops on the southern and northern escarpment of the graben are shown in Figure 2. All surface samples were collected from outcrops in 2018 and the cutting samples during drilling in 2017. While the first location is in Cretaceous marbles (northern escarpment), the latter location is underlain by marble and marble-schist intercalations of Paleozoic age (Régnier et al., 2007) (southern escarpment). The T1 sample originates from a small marble deposit, which is not shown in the map due to scale reasons. A stratigraphical classification of T1 is not possible.

The samples from the southern escarpment are indicated with "Paleozoic" (T13-1 to 4; south of Koçarli village) and from the northern escarpment with "Cretaceous" (T3, T4, T5, T11; vicinity of Köşk village) based on the mapped geological formation (Figure 2). The cutting samples from the GP-1 well are differentiated in shallow ("well^S", 1,050-1,325 m) and deep ("well^D", 3,650-3,870 m) marble-bearing horizons based on intersection.

During drilling (rotary, direct circulation), composite samples of cuttings were taken in 5-m intervals. All samples were lag-time corrected and, after washing and drying, petrographical features were characterized with a binocular directly on site. Eight samples representative of the upper and lower marble-bearing intersections were selected for further analysis.

Ricca et al. (2015) published a methodological approach to differentiate various marble types, originally

named as provenance determination key. After sampling, the marbles were classified as pure or impure calcitic or dolomitic (Supplementary Material 3). Here the approach by Rosen et al. (2007) was applied where a pure calcitic marble is characterized by a modal $CaCO_3$ content of > 95%. The calcite ($CaCO_3$) content of the total cutting sample in vol-% was first determined by point counting using a Novex RZB-SF binocular at drilling site.

Furthermore, we employed a coupled scanning electron microscope and energy dispersive X-ray fluorescence analysis (SEM-EDX) to detect the type and purity of the samples in the Laboratory of the University of Greifswald, Germany. Hand specimens were crushed and attached to aluminium test plates with double side carbon adhesive pads to prevent charging of the sample. Additionally, the surfaces were vapour-coated with carbon. For the cutting samples, the same procedure was applied to 3 to 4 single calcareous grains previously identified under the binocular. A SEM Zeiss Evo 10 with an acceleration voltage of 20 kV was used. The EDX analysis was carried out using an element C2 detector.

A macroscopic characterization of colour, rock texture including shape-preferred orientation, pattern, grain shape, grain structure, maximum grain size and grain size distribution of calcite and dolomite grains, open or sealed fissures and possible weathering features was done in the field and on hand specimens using a hand lens with millimetre scale. The odour while crushing the hand specimens or after reacting with hydrochloric acid (HCl) was determined indicating the presence of accessory pyrite. The light transmission was determined with a focused flashlight in the categories very low to high as described in Cramer (2004). For the cutting samples, these investigations were carried out using a binocular with the exception of fissure and karst features.

Microscopic features were analysed at the drilling site and the thin section analysis of both cuttings and surface samples (T1, T3, T5, 1-1050, 2-1065, 3-1290, 4-1325) with a polarizing microscope at the Karlsruhe Institute of Technology (KIT, Zeiss Axio Scope.A1, Axiocam 105 color). The colouring by Alizarin-S was done to distinguish calcite and dolomite. The thin section description focused on rock type and texture of the cuttings, including shape-preferred orientation and pattern of calcite and dolomite. The maximum grain size and grain size distribution of calcite and dolomite was determined by the conventional linear intercept method (Münzner and Schneiderhöhn, 1953). The average cutting size is in the range of 5 mm and that is why larger grain sizes cannot be investigated for these samples. The mineralogy was quantified by point counting with a binocular and colouring by Alizarin-S.

4.2. ICP-MS and ICP-OES analysis

For geochemical analyses, surface samples were crushed and pulverized in the Laboratory of Environmental and Raw Materials Analysis (LERA), Chair of Geochemistry and Economic Geology (EGG), Institute of Applied Geosciences (AGW) at KIT, while calcareous grains were picked from the cuttings using a binocular. In order to achieve complete digestion, the pulverized samples were dissolved in a combined HNO_3-HF-$HClO_4$ acid digestion. All samples were of suprapur (HNO_3, HF) or normapur ($HClO_4$) quality. The digests were analysed in LERA by inductively coupled plasma optical emission spectroscopy (ICP-OES, Varian 715ES, Agilent) (Ca, Fe, K, Mg, Na, Sr) and by inductively coupled plasma mass spectrometry (ICP-MS, XSeriesII, Thermo Fisher Scientific) with helium and hydrogen as collision gas (trace elements and REE). The collision gas was used to enable an accurate analysis of the interference-critical elements copper (Cu) and zinc (Zn). Quality control was secured by measuring the standard dolomite reference material "JDo-1" (SplitIO/Position 90) of the geological survey of Japan. Overall accuracy was better than ± 10%; however, for some elements (e.g. Rb, Cs, Pb) the accuracy was lower mainly due to their extremely low concentration in carbonates.

REE concentrations including yttrium (REY) data were normalized to the Post Archean Australian Shale standard (PAAS, Piper and Bau, 2013; Y values from Condie, 1993). The calculation of the Ce anomaly is shown in equation (1) (Lawrence et al., 2006).

$$Ce/Ce^* = \frac{\frac{Ce_{sample}}{Ce_{PAAS}}}{((\frac{Pr_{sample}}{Pr_{PAAS}})^2 / \frac{Nd_{sample}}{Nd_{PAAS}})} \tag{1}$$

Furthermore, equation (2) introduces the Pr/Pr* parameter, which is useful to differentiate between apparent and real Ce anomalies (Bau and Dulski, 1996). If samples show a calculated Ce anomaly but Pr/Pr* yield values between 0.95 to 1.05, an apparent Ce anomaly is indicated.

$$Pr/Pr^* = \frac{2 * \frac{Pr_{sample}}{Pr_{PAAS}}}{(\frac{Ce_{sample}}{Ce_{PAAS}} + \frac{Nd_{sample}}{Nd_{PAAS}})} \tag{2}$$

Yttrium anomalies are indicated by calculating the ratio of Y to Ho without normalization (Webb and Kamber, 2000; Tostevin et al., 2016). Europium anomalies are calculated with respect to its neighbours Sm and Gd as demonstrated in equation (3) (Meyer et al., 2012; Tostevin et al., 2016).

$$Eu/Eu^* = \frac{2 * \frac{Eu_{sample}}{Eu_{PAAS}}}{\frac{Sm_{sample}}{Sm_{PAAS}} + \frac{Gd_{sample}}{Gd_{PAAS}}} \tag{3}$$

4.3. Stable carbon and oxygen isotopes

The C and O isotopic composition ($\delta^{13}C$, $\delta^{18}O$) of the marble carbonate minerals was determined by a Finnigan MAT 251 mass spectrometer in the laboratory of the University of Kiel, Germany. Samples reacted in 99% H_3PO_4 to release gaseous CO_2 that was transferred into the mass spectrometer. The calibration was done using the carbonate isotope standard reference materials NBS 18, NBS 19 and 20. The C isotopic composition is given in the delta notation relative to the Vienna Pee Dee Belemnite (V-PDB) standard. O isotope data are given relative to the Vienna Standard Mean Ocean Water (V-SMOW). Measurement precision of repeated isotope measurements were within 0.1 to 0.5 ‰ for both O and C. To convert the $\delta^{18}O$ values from V-PDB to V-SMOW, equation (4) was used (Hoefs, 2015).

$$VSMOW\ in\ ‰ = 1.03091 * VPDB\ in\ ‰ + 30.91 \quad (4)$$

4.4. Rb-Sr geochronology

For Rb-Sr multimineral-based geochronology, we selected impure marble samples with significant amounts of muscovitic white mica and/or biotite. These were the surface sample T13-3 and the cuttings samples 1-1050,

3-1290, 4-1325, 5-3655 and 7-3740. In addition, the $^{87}Sr/^{86}Sr$ isotopic composition of pure marble samples T1, T3, T13-1 and T13-4 was measured. This was done to potentially determine the age of marble deposition from seawater based on Sr isotope stratigraphy (cf. McArthur et al., 2001). Sample preparation and analytical procedures followed the techniques outlined in Glodny et al. (2008a). Isotopic data were measured at GFZ Potsdam on a Thermo Scientific TRITON thermal-ionization mass spectrometer. Strontium data were generated in the dynamic multicollection mode, whereas Rb isotope dilution analysis was done in static multicollection mode. The value for $^{87}Sr/^{86}Sr$ in the NIST SRM 987 isotope standard, as obtained during the period of the analytical work, was 0.710242 ± 0.000020 (2σ, n = 16). Isochron parameters were calculated using standard uncertainties of 0.005% for Sr isotopic ratios and of ± 1.5% for Rb/Sr ratios. Individual analytical uncertainties were consistently smaller than these values. Uncertainties of isotope and age data are stated as 2σ throughout this work. The program ISOPLOT/EX3.71 (Ludwig, 2003) was used to calculate regression lines. The ^{87}Rb decay constant is adopted as suggested by Villa et al. (2015).
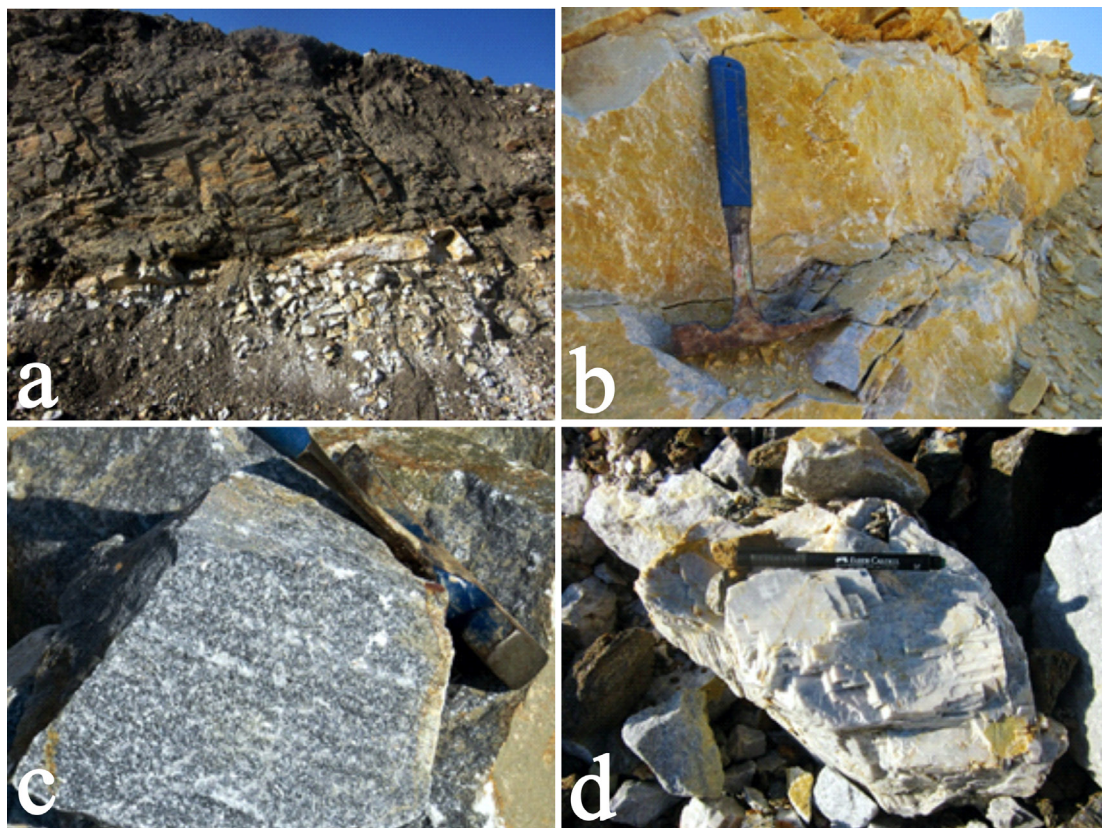
Figure 3. Paleozoic marble: marble quarry SE of Koçarlı village, southern escarpment of the BMG (Location T13): a) banded gneiss (dark colour) on top of marble (light colour) (image width: 6 m), b) light blueish-grey marble, c) light blueish-grey banded marble, d) light grey marble.

5. Results

5.1. Petrography

Paleozoic marble: The Paleozoic marble outcrops at the southern escarpment of the BMG (T13; Figure 2) are characterized by marble, which is overlain by banded gneiss (Figure 3a). The marble is banded or has granoblastic structures (Figure 3c). At the contact of both units, an approximately 40 cm thick layer of very fine-grained marble is found, which shows less than 5 vol-% iron oxides (especially sample T13-3). The main marble horizon is massive, has a fine- to medium grain size and a mostly evenly distributed grain size but partly elongated calcite grains (T13-1, T13-4). Calcite (T13-2) is locally euhedral. Accessory pyrite explains the sulphuric odour while crushing the rocks. Typical for this marble is the light blueish-grey colour, a very low light transmission and a striated, partly mottled pattern. The marble is crosscut by fine carbonate fissures (approx. 1 mm thickness, N-S trending), covered with iron oxides.

The SEM-EDX analysis of carbonate grains of this marble confirms calcite as the dominant carbonate mineral (Figure 4). The only exception is sample T13-3 with a nearly balanced Ca and Mg ratio pointing to an impure dolomitic marble. In the abandoned quarry of T13 location, the T13-3 sample is located very close to the transition to the overlying gneiss sequence (Figure 3a).

Cretaceous marble: The Cretaceous marble is composed of a white marble (Figure 5a and b) at the footwall and alternating marble and meta-marl of approx. Three metres thickness in the hanging wall (Figure 5c). The white marble is predominantly very fine-grained, massive with fine fissures and frequent thin veins, both mainly composed of calcite (Figure 5a). The SEM-EDX analysis confirms calcite being the major carbonate mineral in the white marble. No foliation is observed. In thin section, the white marble has a homeoblastic structure with 75 vol-% calcite and 25 vol-%

dolomite (Figure 6a). The grains are locally fractured with bulged grain boundaries (Figure 6b).

The photomicrographs show a heteroblastic marble of mainly 90 vol-% calcite with some partly rounded and unoriented calcite grains that are embayed in a dark calcitic matrix (Figures 6c, 6d, and 6f). The contact between the calcite grains is dentated. Thin, calcite-filled fissures and stylolites crosscut the calcite matrix (Figure 6e). Samples T1, T3 and T4 display a hematite coating along calcite grain boundaries.

GP-1 well: The GP-1 well intersected two marble horizons which were both sampled (Figure 7). Due to the drilling technology, all cutting samples are composite samples from a depth interval of 5 m. At bottom hole, orthogneiss with eclogite intercalations was drilled. Above this, the deepest carbonate-bearing rock section was sampled and further analysed (8-3865). It is a fault-related alteration zone having a significant calcite content (Figure 7) of 10 vol-% with also chips of orthogneiss and eclogite. The calcite content is rather low compared to the other cutting samples (Table 1). Above the fault, a mixed layer of predominantly banded gneiss and orthogneiss is present with fault-controlled hydrothermal alteration zones in various intersections.

The samples of the deep marble horizon show alternating layers of marble and banded gneiss at a decimetre scale, sometimes intercalated by feldspar-quartz veins. The calcite content is in the range of 32 to 41 vol-% (Table 1). The colour is white to light grey with a very low light transmission. The grain size is equally fine-grained. Calcite is characterized by partly elongated twin lamellae with dentated and sometimes lobate grain boundaries (Figure 8a). The EDX investigation yields more than 90 vol-% Ca content for the samples 6-3680 and 7-3740. This horizon is characterized as impure calcitic marble.
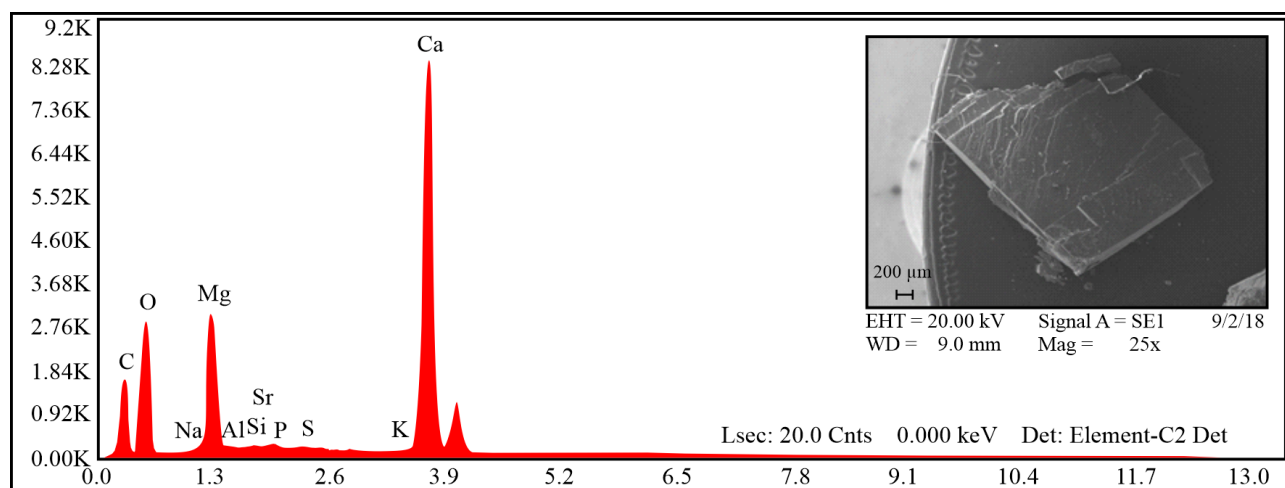
Figure 4. SEM-EDX of sample T13-2. It shows that Ca is the main constituent of the sample.
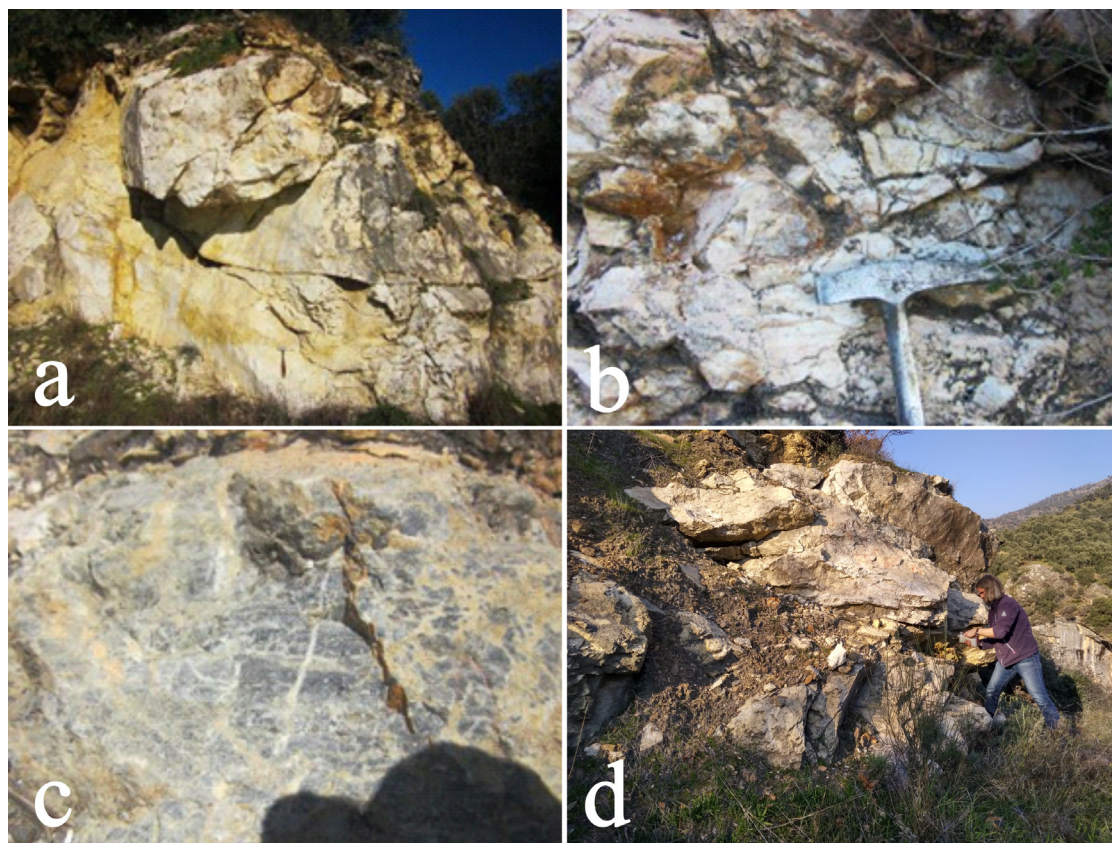
Figure 5. Marble of three different outcrops at the northern escarpment of the BMG between Köşk and Eğrikavak (Figure 2). a) Characteristic outcrop of the Cretaceous massive marble showing a light-coloured marble (T3) (image width: 10 m). b) Detail of a) highlighting the characteristic white colour of the Cretaceous marble. c) Typical metamorphosed marl of a Cretaceous unit showing the cross-hatched pattern of calcite veins (T5) (image width: 0.2 m), d) characteristic white marble of outcrop T11 with an overlying clay sequence.

The shallow marble horizon above a fault-related alteration zone with greenish clay has a calcite content of 39 vol-% (sample 4-1325; Table 1). Shallower intersections (sample 3-1290) have similar characteristics with small interbedded layers of biotite gneiss. The marble consists of mainly calcite and little dolomite with bulged grain boundaries (Figure 8b).

In the upper layer, a fault-related alteration zone is intersected, which is adjacent to alternating layers of marble and banded gneiss. This section is followed by muscovite schist and meta-greywacke. At a depth of 1,065 m, a marble section with alternating layers of marble and banded gneiss is present. This marble has a blueish to light grey colour along with a low to medium light transmission and striated patterns. It has a calcite content of 56 to 75 vol-% (Table 1, 1-1050 and 2-1065) and a granoblastic-polygonal texture (Figure 8c) with fine-grained, elongated calcite grains. Compared to the other cutting samples, this marble has the highest calcite content. The sample 1-1050 has additional calcite fissures.

Marble from the shallow intersection contains a small amount (< 5%) of quartz and mica.

Maximum grain size of carbonate minerals in Paleozoic, Cretaceous and GP-1 samples: The maximum grain size (MGS) of the calcite and dolomite varies in a comparatively small range between 0.2 and 3.0 mm (Figure 9). One outlier is the Paleozoic outcrop sample T13-2 with an MGS > 10 mm (Supplementary Material 4). The MGS of the well samples appears to be small compared to the surface samples, but no systematic difference is observed and the cutting size of ~5 mm may have influenced the MGS determination of the well samples. The MGS of the samples analysed are small in comparison to data published from other sites worldwide ranging from 0.2 mm to 9.5 mm (Gorgoni et al., 1998; Ricca et al., 2015; Figure 9).

5.2. Geochemistry
Major and trace elements: All samples collected at outcrops are dominated by a high CaO content of 33 to 59 wt-%
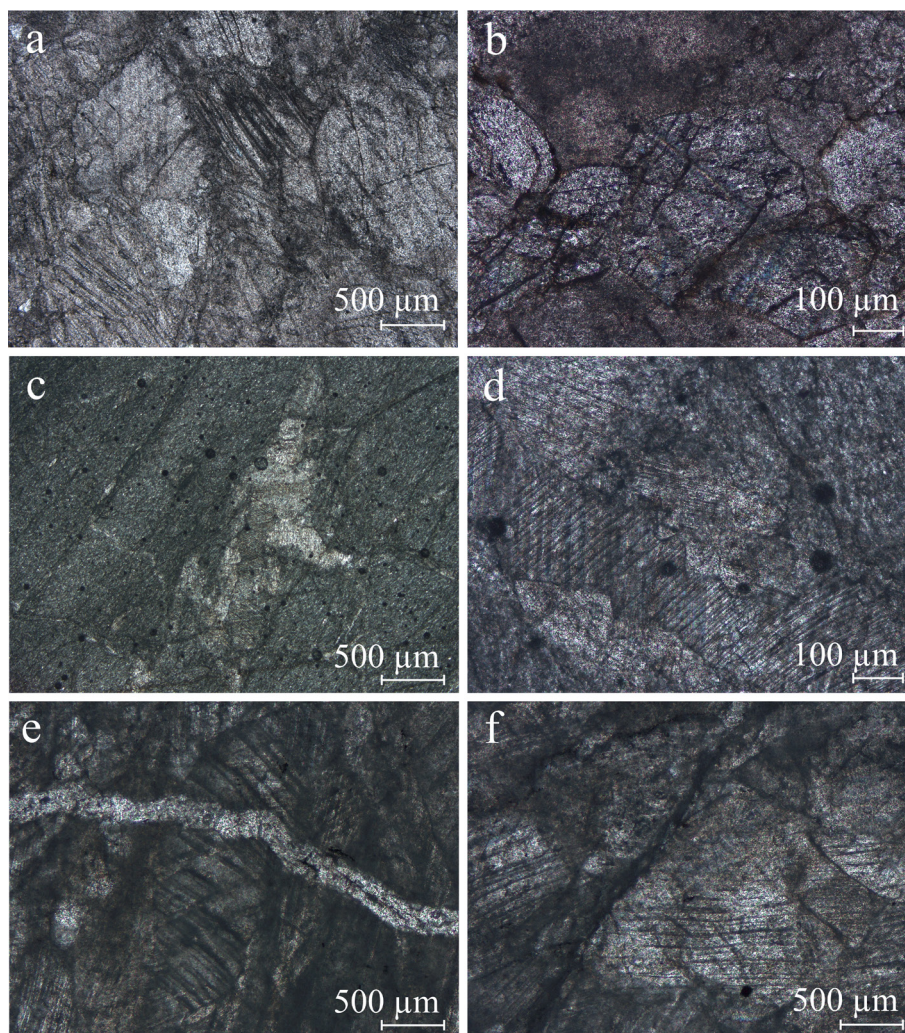
Figure 6. Representative photomicrographs of Cretaceous marble (T1, T3 and T5). The dark and blurred appearance of thin sections is caused by poor polishing and a slightly higher thickness than standard. a) Mainly homeoblastic calcite with twin lamellae parallel to the rhomb edges in plane polarized light (ppl). The sample consists of ca. 75 vol-% calcite and 25 vol-% dolomite (T1), b) fractured calcite of T1 in detail (ppl), c) calcite grains in calcite matrix with twin lamellae representing a heteroblastic marble of ~90 vol-% calcite (ppl) (T3), d) fractured calcite with abundant twin lamellae (ppl) (T3), e) calcite fissure in calcite matrix showing twin lamellae (ppl) (T5), f) thin section with approximately 90 vol-% calcite and fractured calcite grains (ppl) (T5).

(Supplementary Material 5). The Paleozoic marble has CaO contents in the range of 50 wt-%; however, the T13-3 sample shows a lower CaO content of 33 wt-% along with a higher MgO content of 19 wt-%. The CaO content in the Cretaceous marble lies within the same range (Supplementary Material 5). Both the Cretaceous and the Paleozoic samples show a similar pattern when they are compared in terms of the concentrations of the major elements (Figure 10a). The Na_2O and K_2O contents are mostly below the detection limit (Figure 10a). All samples of the Paleozoic and Cretaceous marbles have similar Al_2O_3 (0.02 wt-%–0.87 wt-%), $Fe_2O_{3\ tot}$ (0.07 wt-%–1.34 wt-%) and MnO (0.01 wt-%–0.15 wt-%) concentrations. The Sr concentration is below 1,000 mg/kg in the outcrop material.

The trace element concentrations of the Paleozoic and Cretaceous marble are rather low with a sum of below 460 mg/kg (Li to U, Supplementary Material 5). Beside Sr, Ba, and P partly show higher concentrations in the range from 5 to 220 mg/kg. Based on the major and trace element concentrations, the Paleozoic and Cretaceous marbles are indistinguishable (Figure 10a).

The well[s] samples of GP-1 have similar but lower CaO contents compared to the outcrop material with a slightly lower average content of 44 wt-%. Compared to the deeper section below 3,000 m depth, the well[s] samples exhibit higher CaO content (Figure 10b). The Al_2O_3, $Fe_2O_{3\ tot}$ and MnO concentrations of the well[s] samples are also similar to the outcrop samples, whereas the Na_2O and K_2O concentrations

1017
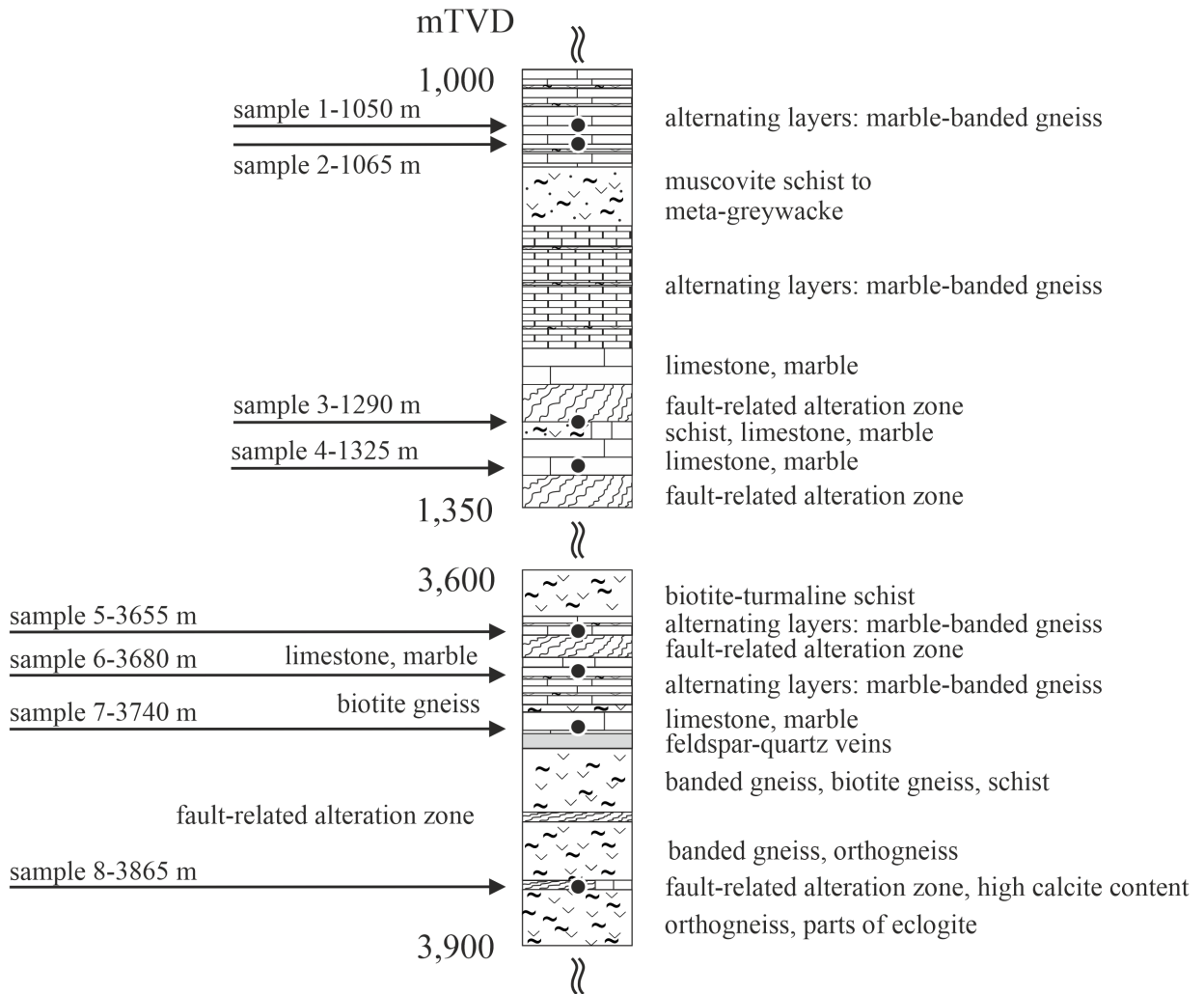
Figure 7. Marble-bearing sections of the geothermal exploration well GP-1. Samples for detailed analysis are marked. Above 1,000 m, the sedimentary cover was drilled. In between the marble horizons gneiss and schist sequences were drilled, below 3,900 m a 50 m orthogneiss horizon was drilled until bottom hole. mTVD: metres in total vertical depth.

Table 1. Calcite content as a result of point counting of the sampled cuttings. mTVD: metres in total vertical depth.

Name	Origin	Depth	Calcite content
		(m TVD)	vol-%
1-1050	well[S]	1,050	75
2-1065	well[S]	1,065	56
3-1290	well[S]	1,290	34
4-1325	well[S]	1,325	39
5-3655	well[D]	3,655	39
6-3680	well[D]	3,680	32
7-3740	well[D]	3,740	41
8-3865	well[D]	3,865	10

reach partly 3–18 times higher concentrations than in the outcrop samples. The Sr concentrations reach up to 2,274 mg/kg. Besides Sr, the well[S] samples have a sum of trace element contents of P, V, Cr, and Ba below 400 mg/kg. The total trace element content (Li to U, Supplementary Material 5) is higher than in the outcrop samples.

The well[D] samples show a different major element pattern (Figure 10b) than the Paleozoic and Cretaceous outcrop samples and well[S] samples. This is mainly related to Na_2O, K_2O and Al_2O_3 concentrations that are approximately one order of magnitude higher and within a range from 1 to 17 wt-%. The Sr concentrations are below 455 mg/kg. However, the total trace element content is relatively high with 1,265 mg/kg to nearly 3,000 mg/kg. In general, the cutting samples have higher trace element content than the outcrop samples.
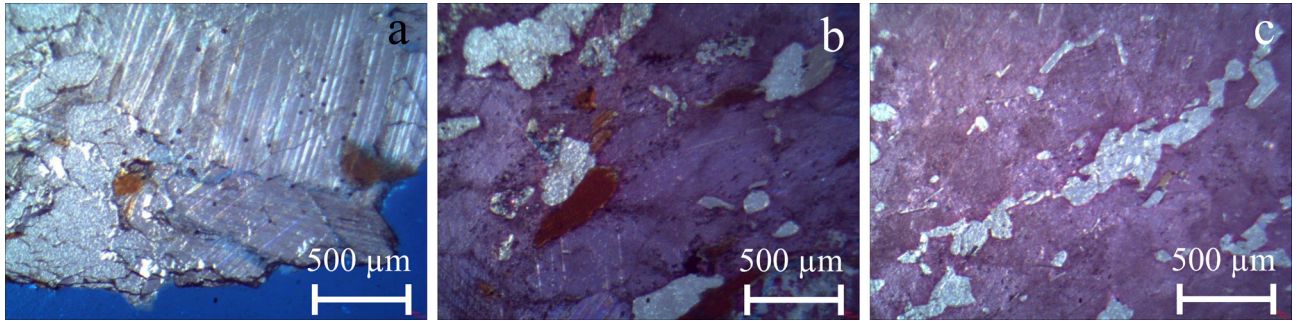
Figure 8. Representative photomicrographs of cutting samples of the GP-1 well, b)-c) sections coloured by Alizarin-S: a) thin section of cuttings from 3,740 m with typical twin lamellae in partly elongated calcite with dentated and lobate grain boundaries (ppl), b) thin section of cuttings from 1,290 m containing mainly calcite and little dolomite (ppl), c) thin section of cuttings from 1,050 m with reddish calcite having a granoblastic-polygonal texture (ppl).
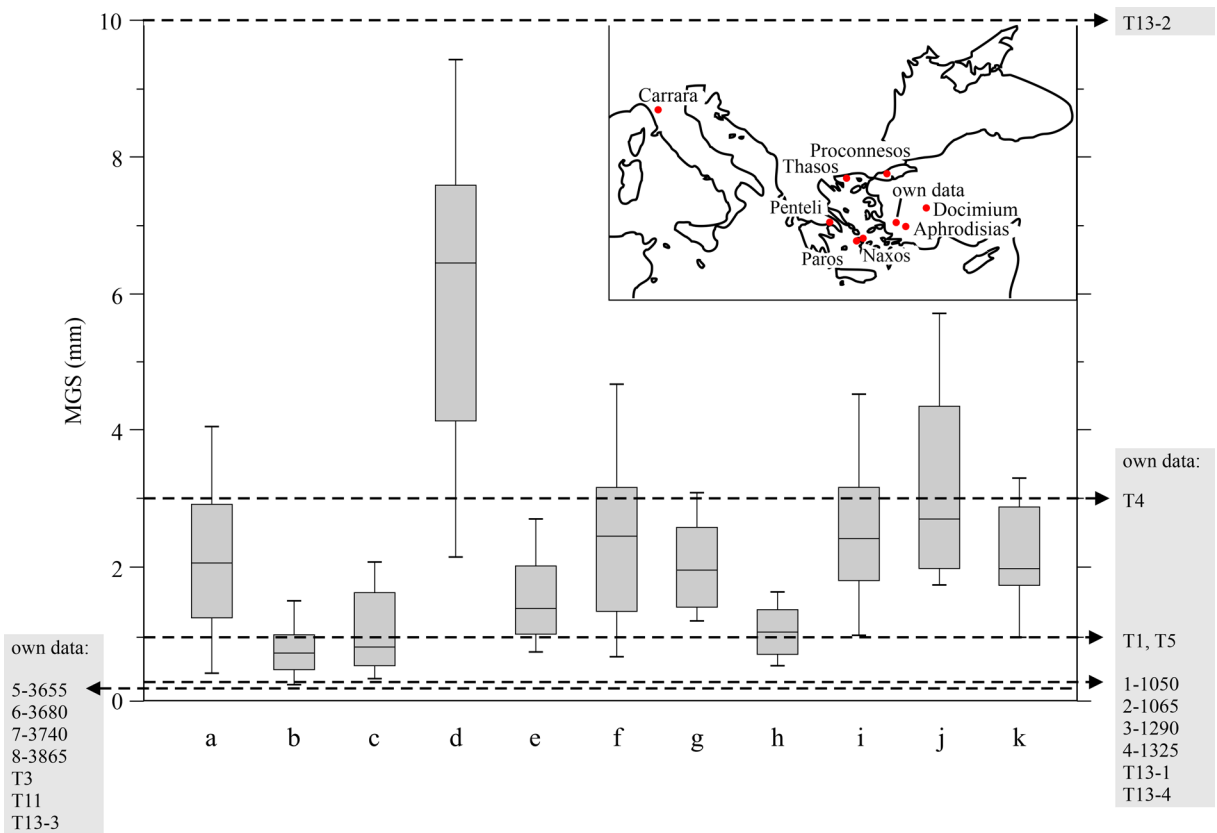
Figure 9. Comparison of maximum grain size of various marbles (this study and Gorgoni et al., 1998). a) Aphrodisias, b) Carrara, c) Docimium, d) Naxos, e) Paros (1), f) Paros (2), g) Paros (4), h) Penteli, i) Proconnesos, j) Thasos (2), k) Thasos (3). The literature data is not from the same stratigraphy as the samples of this study.

REY geochemistry: The Paleozoic marble samples tend to slightly lower REY content (normalized to PAAS) compared to the Cretaceous samples (Figure 11). They lie within the range of the Menderes region with a negative Ce (0.68-0.71) and a positive Y anomaly (Y/Ho ratio: 39–48) (c.f. Cramer, 2004). Each sample of Cretaceous marble has a negative Ce (0.55–0.80) and a positive Y anomaly (Y/

Ho ratio: 44-51) (Figure 11). In addition, the T3 and T4 samples have a positive Eu anomaly (2.54 and 1.27) and also have higher normalized La to Tb values than reported for the Menderes region published by Cramer (2004).

The GP-1 samples generally show higher absolute and normalized REY values in comparison with the surface samples (Figure 11). The well[D] samples show higher
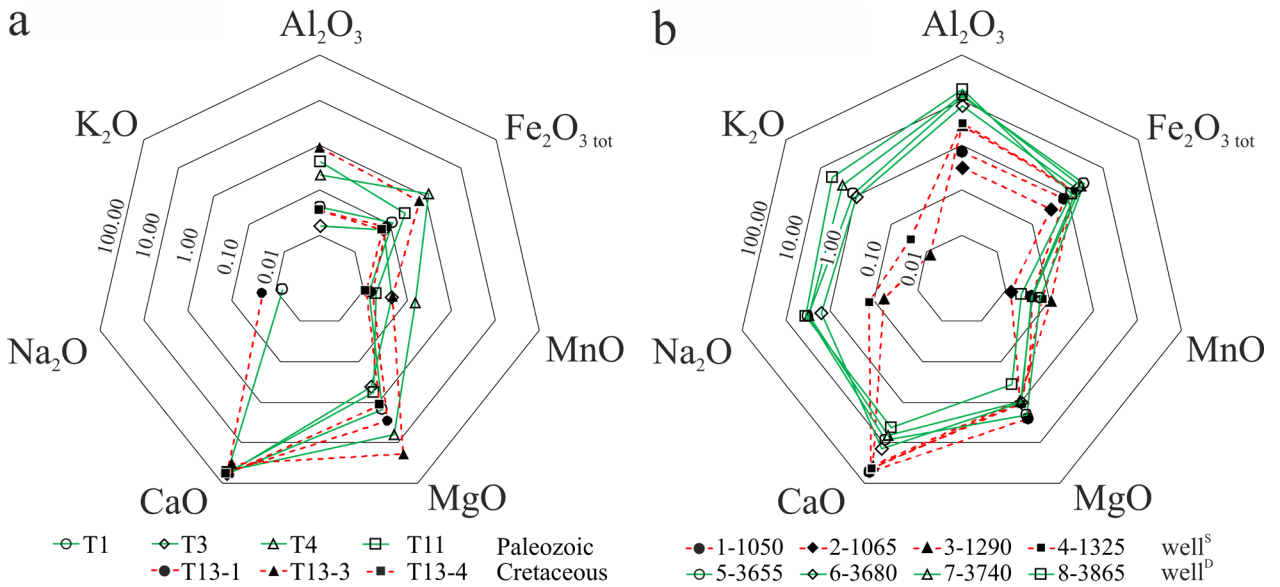
Figure 10. Major oxide geochemistry in wt-%. a) surface samples (Paleozoic, Cretaceous), b) cutting samples (well[S]; well[D]).
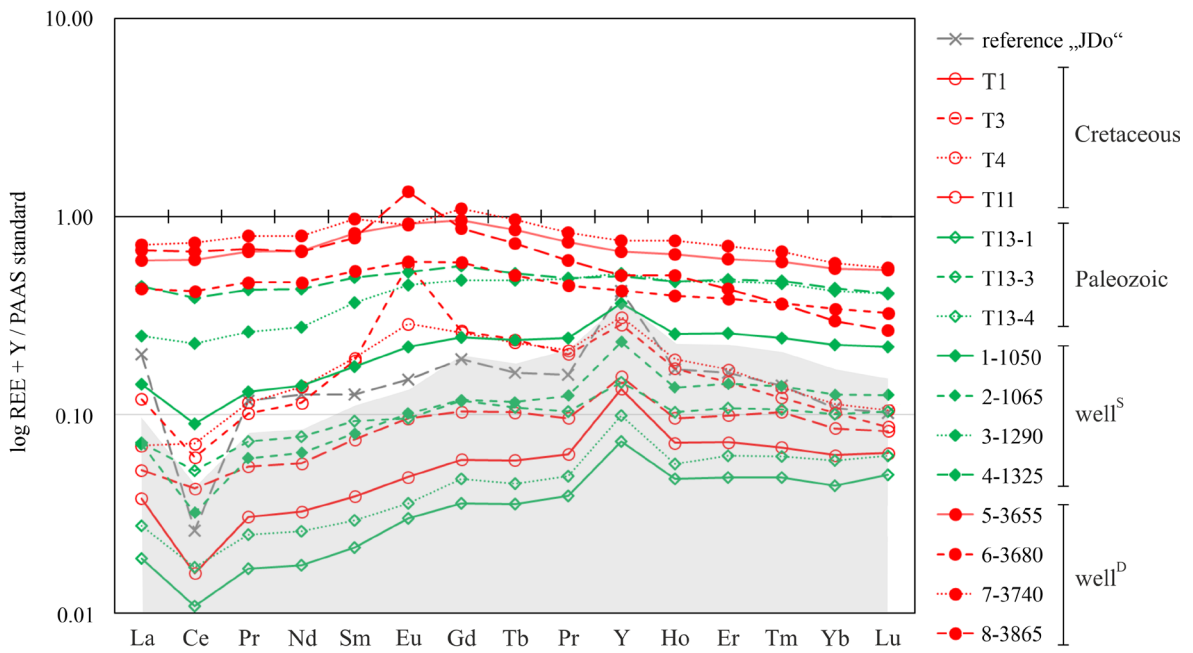
Figure 11. PAAS-normalized Y and REE patterns for cutting and surface samples. The grey shaded area indicate maximum values reported for the Menderes region (Cramer, 2004). Minimum values of Cramer (2004) are lower than the shown normalized value of 0.01.

absolute and normalized values than the well[S] samples, which have normalized values below 0.6. The samples 1-1050 and 2-1065 have strong negative Ce anomalies with Ce/Ce* values of 0.73 and 0.56 and Y/Ho ratios of 39 and 46, respectively. The samples 3-1290 and 4-1325 have only a slight Ce anomaly (0.92–0.93) and no distinct Y anomaly (Y/Ho ratio: 29 and 30). The well[D] cuttings have a flat

PAAS-normalized pattern between La and Ho and neither a Ce nor a Y anomaly (Y/Ho ratio: 27–29) (Figure 11). Sample 8-3865 has a distinct positive Eu anomaly (1.62). In comparison to the cutting samples, the surface samples have a stronger Ce anomaly.

Regarding their absolute REY values, Paleozoic and well[S] samples show lower REY contents than well[D]

samples and Cretaceous marble. In addition, the well[D] and Cretaceous samples exhibit higher PAAS-normalized Gd_{PAAS}/Lu_{PAAS} (Lu: lutetium) ratios (Figure 12). The Paleozoic and the well[S] samples have a lower Gd_{PAAS}/Lu_{PAAS} ratio indicating no significant HREE decrease.

Carbonate stable isotope composition: $\delta^{18}O$ and $\delta^{13}C$: The $\delta^{13}C$ values show a range from 1.73 to 4.25 ‰ for the Paleozoic marble and –0.42 to 4.40 ‰ for the Cretaceous marble (Supplementary Material 6). The well[S] samples have $\delta^{13}C$ values from 1.76 to 3.00 ‰ and the well[D] samples show negative values from –2.89 to –1.57 ‰. The $\delta^{18}O$ values in the Paleozoic samples are in the range of 19.62 and 23.84 ‰ and those of the Cretaceous samples in the range of 6.74 to 21.11 ‰. Well[S] samples have $\delta^{18}O$ values between 18.17 to 20.07 ‰ and the well[D] samples values between 13.05 and 15.28 ‰, respectively.

All Paleozoic and well[S] samples show higher $\delta^{13}C$ values (1.73 to 4.00 ‰) relatively to well[D] and Cretaceous samples (–2.89 to 1.60 ‰) (Figure 13). The only exception is sample T1 (Cretaceous) with the highest $\delta^{13}C$ value of 4.40 ‰. The well[D] and Cretaceous samples show lower $\delta^{18}O$ values (6.74 ‰ to 15.28 ‰) than the Paleozoic and

the well[S] samples (18.17 ‰ to 23.84 ‰) with values less than 15.28 ‰, except T1 sample (Cretaceous), which has a $\delta^{18}O$ value of 21.11 ‰ (Figure 13). The Cretaceous samples T3 and T5-1 show $\delta^{18}O$ values below 10 ‰. Both, cutting and surface samples of Paleozoic and well[S] form one group regarding the ranges of the $\delta^{13}C$ and $\delta^{18}O$ values. Similarly, the Cretaceous and well[D] samples can be grouped together (Figure 13).

In general, the $\delta^{13}C$ values of this study are in a similar range compared to the samples from the Menderes region (from –6 to 5 ‰; Cramer, 2004; Manfra et al., 1975). The range of $\delta^{18}O$ values from the investigated well[S] and Paleozoic samples are within the proposed range for limestone and marble (c.f. Rollinson, 1993). The Cretaceous and well[D] samples are significantly depleted in [18]O compared to the limestone-marble range specified by Rollinson (1993) (Figure 14a).

The $\delta^{13}C$ signature of Cretaceous and well[D] samples plot within the field of freshwater as well as marine carbonate rocks, whereas Paleozoic and well[S] samples show higher values within the freshwater carbonate rock region, some even exceeding towards higher values (esp. Paleozoic;
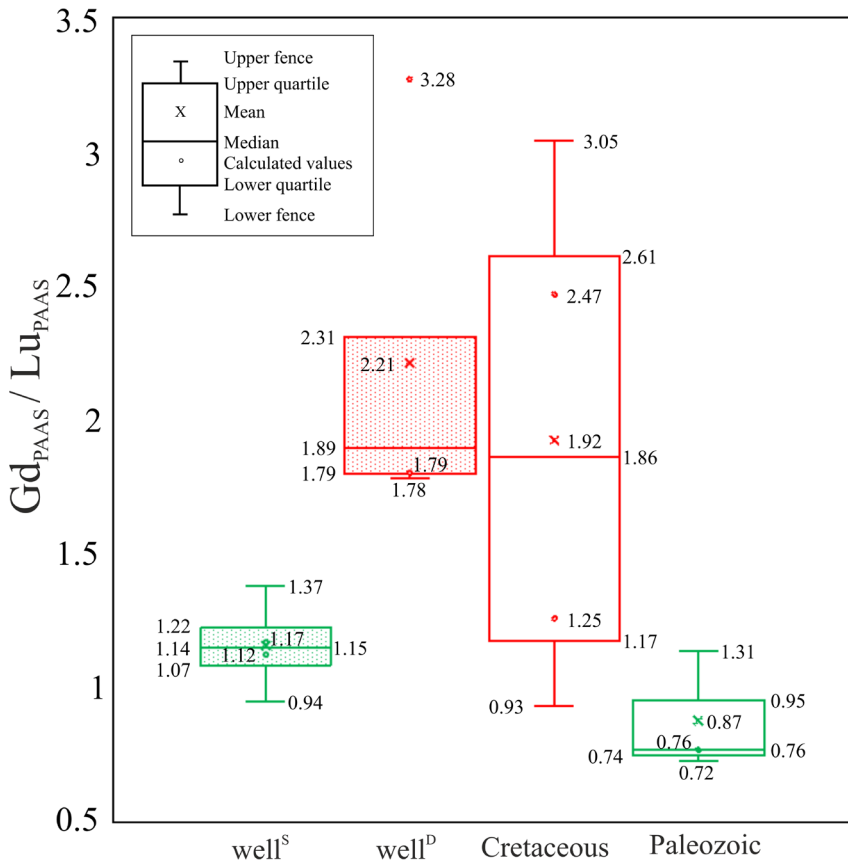
Figure 12. Boxplot showing the PAAS-normalized values and quartiles of Gd_{PAAS}/Lu_{PAAS} ratios. The diagram displays the decrease of $HREE_{PAAS}$ in the well[D] and Cretaceous samples.
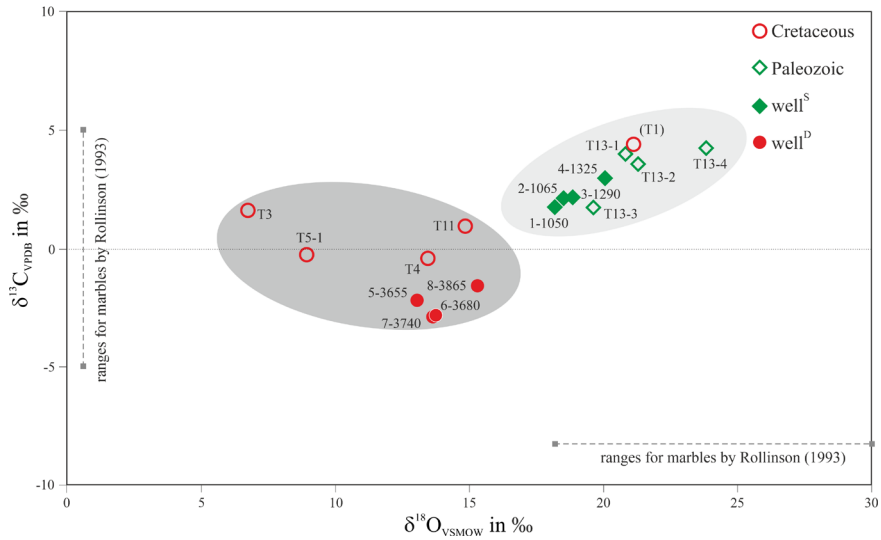
Figure 13. Cross plot of $\delta^{18}O$ and $\delta^{13}C$ isotopic signatures. The grey ellipses indicate two groups according to the isotopic composition and define the well[D] and the Cretaceous samples as one group and the Paleozoic and well[S] samples, respectively.
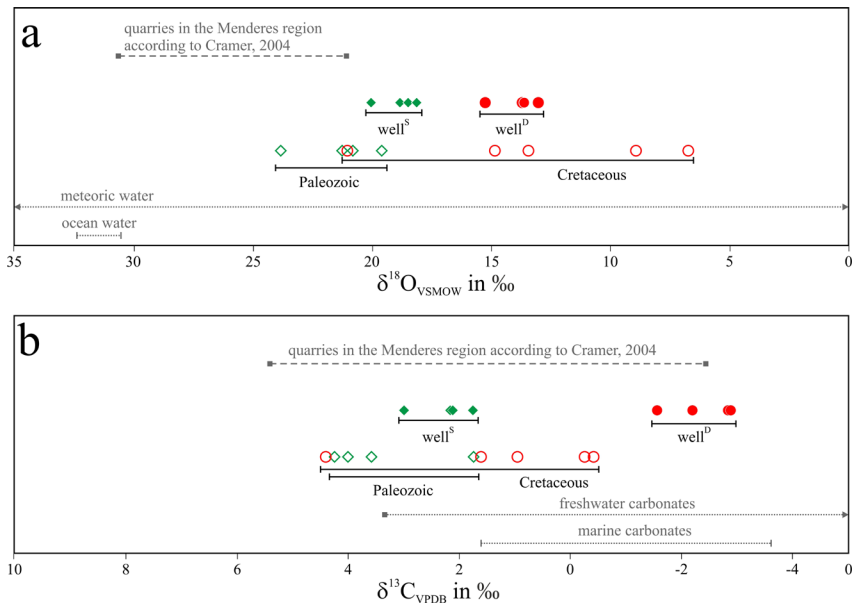
Figure 14. a) $\delta^{18}O_{VSMOW}$ isotopic values and b) $\delta^{13}C_{VPDB}$ in ‰ from the samples in this study in comparison with common ranges of different rocks and waters (modified after Hoefs, 2015).

Figure 14b). In contrast to $\delta^{13}C$, the $\delta^{18}O$ values show a wider spread. The $\delta^{18}O$ values of all samples plot in the meteoric water region. They display relatively low values of $\delta^{18}O$ compared to other samples from the Menderes region (Cramer, 2004).

Rb-Sr geochronology and $^{87}Sr/^{86}Sr$ data: Six samples in total were analysed for Rb-Sr multimineral systematics (Figure 15; Supplementary Material 7). Among the surface samples, only the fine-grained marble of sample T13-3 had sufficient mica to determine a Rb-Sr age (Figure 15a). The data for calcite and two muscovitic white mica fractions do not define an isochron; however, ages calculated for the two calcite-white mica pairs are close to 30 Ma (30.72 ± 0.46 Ma and 27.75 ± 0.47 Ma).
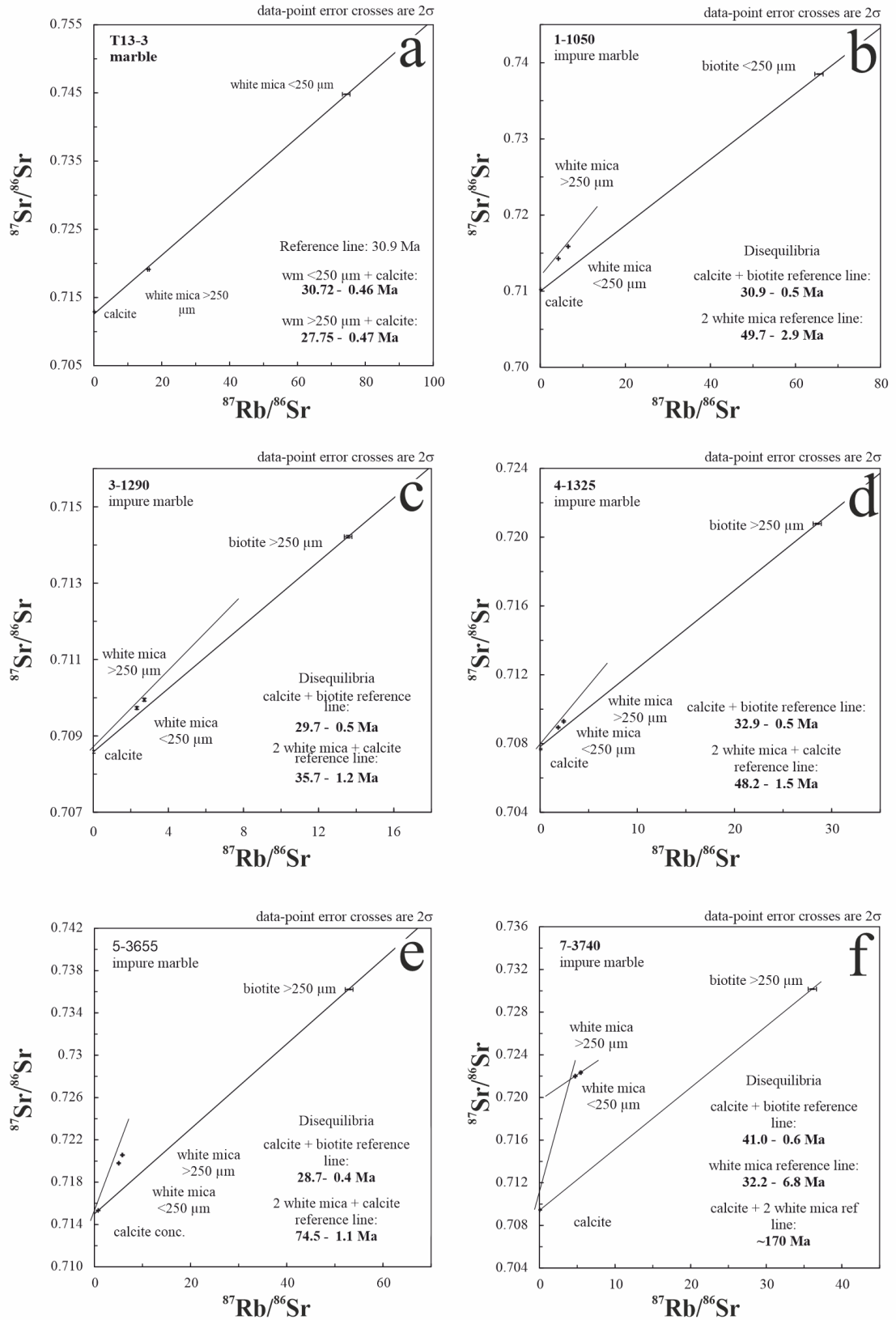
Figure 15. Rb-Sr isochrons. Age results by calcite-biotite and white mica-calcite reference lines of the samples a) T13-3, b) 1-1050, c) 3-1290, d) 4-1325, e) 5-3655, f) 7-3740.

For the five cutting samples, the degree of overprint by ductile deformation was difficult to estimate. Nevertheless, all the samples show indications for a preferred orientation of mica, indicating that the rocks experienced ductile shear. For all these samples, we analysed calcite, two grain size fractions of white mica, and carefully selected, well preserved biotite without any evidence of bleaching or chloritization. A striking similarity between the samples 1-1050, 3-1290, 4-1325 and 5-3655 (Figure 15b, c, d, e) is that calcite-biotite pairs consistently yield apparent ages near 30 Ma, whereas white mica-calcite apparent ages are unsystematically higher, with age values between ~36 and 75 Ma (Figure 6). In sample 7-3740 (Figure 15f), the biotite-calcite age is, with 41 ± 0.6 Ma, apparently older than in the other cutting samples. In this sample, the apparent ages for calcite-white mica pairs are near 170 Ma, being the oldest in the entire set of samples.

The $^{87}Sr/^{86}Sr$ isotopic composition of four samples of pure marble from surface outcrops do not show a consistent cluster but show variable values between 0.7083 and 0.7123 (Supplementary Material 7). A similar variability is seen in the initial Sr isotopic composition of the samples characterized by Rb-Sr geochronology. Here, the initial Sr isotopic composition (as approximated by the Sr isotopic composition of the low-Rb/Sr phase calcite) is between 0.7077 (sample 4-1325) and 0.7153 (sample 5-3655) (Figure 15; Supplementary Material 7). It is important to note that the majority of these initial Sr isotopic ratios are considerably higher than the $^{87}Sr/^{86}Sr$ ratio of seawater in Paleozoic to Mesozoic times (cf. McArthur et al., 2001).

6. Discussion

6.1. Comparison and stratigraphic correlation of cuttings with Paleozoic and Cretaceous marble from outcrops

A synthesis of all investigated petrographical properties (Supplementary Material 4) of the samples reveals that the colour of the marbles is a characteristic macroscopic feature, which allows a subdivision of the examined marbles into two different groups: (1) the marbles from the outcrop south of Koçarlı village (Paleozoic) and from the shallow marble-bearing section in the exploration well GP-1 (well[S]), which are predominantly white; in contrast, (2) the marbles from the outcrops of the northern escarpment of the BMG (Cretaceous) and from the deeper section of the well (well[D]) are characterized by blueish light grey colour (Supplementary Material 4 and 8). The light transmission and different patterns indicate the same two groups and confirm the correlation of cutting and surface samples based on a characteristic colour.

The major elements of all samples except well[D] samples are similar and characterize the marbles as calcitic (Figure 10). Only in the Paleozoic marble, an approximately 0.4 m thick layer of dolomitic marble occurs (Supplementary

Material 8). All well[D] samples plot in a group, which is separated from all other samples by their relatively high $Fe_2O_{3\ tot}$, Al_2O_3, Na_2O and K_2O content in combination with relatively low CaO concentration (Supplementary Material 9). This is explained by a contamination of the cutting samples by schist or gneiss fragments. The geochemistry of the samples from well[S] is more widely scattered than that of the other marble units (Figure 10; Supplementary Material 5).

A mixture of marble with silicate rocks in the deep section of GP-1 is likely since the stratigraphy in the deeper parts is much more variable than in the 1,050–1,325 m section (Figure 7). The deeper reservoir of the geothermal sites in the BMG is mostly an intercalation of marble, schist, and gneiss (Aksoy, 2014; Karamanderesi, 2013). The Cretaceous marble is located at the contact of the shallow south-dipping Büyük Menderes detachment and can occur as intercalation of marble, schist and gneiss sequences (Özer and Sözbilir, 2003).

The well[D] and Cretaceous samples show highest absolute REY and ΣREY values and a high Gd_{PAAS}/Lu_{PAAS} ratio (Figure 12). Additionally, these samples exhibit higher absolute HREE values but with a decreasing trend towards higher masses, which can be explained by pronounced weathering (Pereira et al., 2019). The Paleozoic and well[S] samples do not show this characteristic REY pattern.

Due to contamination, a direct comparison of the absolute REY values of the well[D] samples with the other marble horizons can only be made with restrictions. The normalized REY pattern (Figure 11), and Gd/Lu ratio (Figure 12) can be used as indications allowing a distinction between Paleozoic and well[S] samples relative to the Cretaceous and well[D] samples. All the $\delta^{13}C$ values of this study lie within the general range of marble values (Rollinson, 1993; Cramer, 2004), whereas the $\delta^{18}O$ values are in the lower range of marbles in general (Figures 13 and 14). The Paleozoic and well[S] samples have both higher $\delta^{18}O$ and $\delta^{13}C$ values in comparison to the Cretaceous and well[D] samples. A pronounced CO_2 degassing during metamorphic processes such as decarbonation reactions can explain this difference (Cramer, 2004; Hoefs, 2015). During metamorphic volatilization reactions, the lost CO_2, and additionally H_2O, are enriched in ^{16}O compared to the bulk rock (Valley, 1986; Hoefs, 2015). The well[S] samples have slightly lower $\delta^{13}C$ and $\delta^{18}O$ values than the surface samples, which may be explained by hydrothermal alteration as metamorphic or meteoric fluids lead to decrease of the heavy isotope (Cramer, 2004; Craig and Craig, 1972).

The Cretaceous marble and well[D] samples show in general lower values for both $\delta^{18}O$ and $\delta^{13}C$. They may have been influenced by meteoric water in addition to marine water, so that the limestone protolith had a lighter

pre-metamorphic isotope ratio (Valley, 1986). McCrea (1950) and Kim and O'Neil (1997) investigated the temperature dependence of Ca-carbonate formation on O-isotope composition, yielding decreasing $\delta^{18}O$ values in Ca-carbonate with increasing temperatures. Again, subsequent fluid-rock interaction can be one reason for the lower $\delta^{18}O$ values as explained above. Therefore, no clear correlation of the metamorphic grade and isotopic signature can be made. Combining the $\delta^{18}O$ and $\delta^{13}C$ values (Figure 13; grey ellipses), two groups of marble (Paleozoic and well[S]; Cretaceous and well[D]) are distinguished (Figure 13; Supplementary Material 9). The difference between the two groups is caused by their different metamorphic overprint resulting in different C and O isotopic fingerprint just discussed.

Based on the detailed petrographical and geochemical data (Supplementary Materials 8 and 9), a stratigraphic correlation of cuttings and outcrop samples is suggested. The critical parameters are colour, transparency (light transmission), the REY pattern and stable C and O isotopic composition. The well[S] and the Paleozoic marble are associated to each other, thus both belonging to the Selimiye nappe. Accordingly, the well[D] and the Cretaceous samples are interrelated, belonging to the Bayındır nappe. This implies that the younger Bayındır nappe (e.g. Lips et al., 2001) lies structurally below the older Selimiye nappe (cf. Régnier et al., 2003) intersected by the GP-1 well in the graben structure.

6.2. Implications on marble genesis
The Paleozoic marble shows negative Ce anomalies pointing to a seawater origin and oxic conditions during formation (Figure 16). The positive Y anomalies of the Paleozoic samples indicate a seawater influence (Bau et al., 1997; Tostevin et al., 2016). The negative Ce anomalies and Pr/Pr* indication of the well[S] samples point to a near shore (3-1290 and 4-1325 with Y/Ho ratios around 30) to open marine setting (1-1050 and 2-1065 with Y/Ho 39 and 46). In contrast, the C and O isotopic signatures of the Paleozoic marble samples postulate a meteoric origin of the limestone precursor (Table 2). As subsequent fluid-rock interactions affected the original isotopic signature, the presumed meteoric origin may be biased.

The Cretaceous marble has a positive Y anomaly with highest Y/Ho ratios between 44 and 51 suggesting seawater origin (Bau et al., 1997; Tostevin et al., 2016). The $\delta^{13}C$ values are consistent with both, a seawater, and a freshwater origin (Table 2). The Ce/Ce* values around 0.9, and Pr/Pr* values around 1.0 of well[D] samples indicate oxic conditions during formation of the marble (Bau and Dulski, 1996) (Figure 16).

As the Cretaceous and Paleozoic limestone protoliths formed on the shelf of the Neotethys, they must be marine (Şengör and Yilmaz, 1981; Cramer, 2004; van Hinsbergen
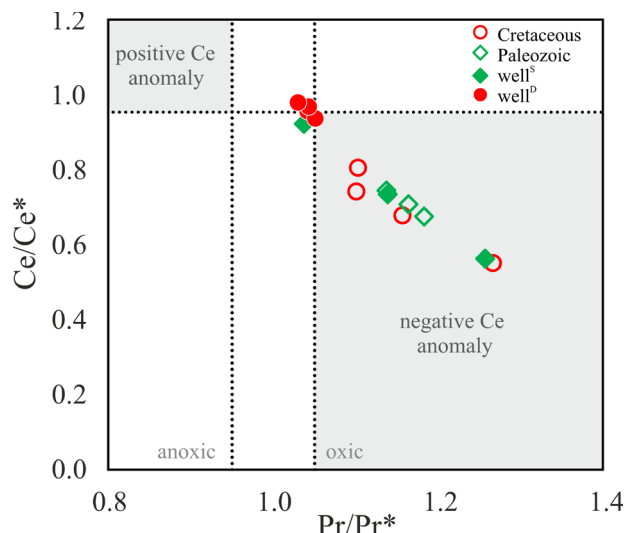
Figure 16. Ce/Ce* vs. Pr/Pr* with Ce anomalies indicated in grey including the marked fields of positive and negative Ce anomalies as described in Bau and Dulski (1996).

et al., 2010; Gessner et al., 2013). Özer and Sözbilir (2003) find Cretaceous reef-forming rudist species which confirm a shallow ocean setting at least for the Cretaceous marble. Thus, the C and O isotopic signatures indicative of meteoric influence, must result from processes that took place during diagenesis or metamorphism.

A strong post-depositional metamorphic overprint is indicated by metamorphic phases within the impure marbles, including biotite and muscovitic white mica. The calcite-biotite Rb-Sr ages clustering around the 30 Ma metamorphic age indicate metamorphic isotope re-equilibration. The C and O isotopic composition may also be influenced by equilibration during metamorphism or interaction with hydrothermal fluids as indicated by abundant veins.

6.3. Structure and evolution of the BMG
The results of this study indicate the location of Cretaceous marble below Paleozoic rocks at the location of the exploration well GP-1 (Figure 2). This is explained by nappe stacking as also suggested by various researchers for the Menderes Massif (Lips et al., 2001; Gessner et al., 2013; Régnier et al., 2003; van Hinsbergen et al., 2010). The two different marble horizons in GP-1 belong to the Bayındır nappe (Cretaceous marble, 3,650-3,870 m) and the Selimiye nappe (Paleozoic marble, 1,050–1,325 m) according to our results from petrographical and geochemical analyses. Consequently, the BMG can be considered as a half-graben structure as already suggested by van Hinsbergen et al. (2010) (Figure 17). In the northern escarpment of the BMG, the four nappes are north-vergent and in the south, the nappes are south-vergent and, separated in blocks

Table 2. Information gained by applying REY and C and O isotopic signatures regarding formation environment.

Geochemical parameter	Ce/Ce* and Y/Ho	$\delta^{18}O_{VSMOW}$	$\delta^{13}C_{VPDB}$
reference	Bau and Dulski, 1996; Webb and Kamber, 2000; Tostevin et al., 2016	Hoefs, 2015	Hoefs, 2015
Paleozoic	oxic, near shore to open marine setting	meteoric water	higher values than freshwater carbonates
well[S]	oxic, near shore to open marine setting	meteoric water	freshwater carbonates
Cretaceous	oxic, seawater	meteoric water	freshwater carbonates and marine carbonates
well[D]	oxic, near shore setting	meteoric water	freshwater carbonates and marine carbonates
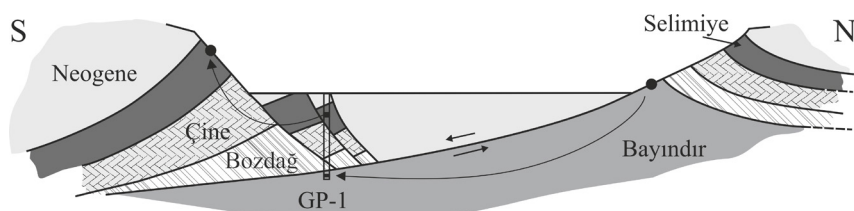
Figure 17. Simplified cross-section of the BMG as half-graben structure with allocated nappes and the exploration well GP-1. The two different marble horizons are marked. The straight arrows indicate the shear sense along the low-angle Büyük Menderes detachment. Complemented and redrawn according to van Hinsbergen et al. 2010.

dipping northwards due to the antithetic normal faults of the graben structure. During graben development, the blocks of Selimiye, Çine, and Bozdağ nappes subsided in the southern graben structure. The deeper marble of the Bayındır nappe is separated by the low-angle, southward dipping Büyük Menderes detachment and represents the deeper (well[D]) marble horizon (Figure 17).

Constraints on the timing of the regional tectonic evolution come from the Rb-Sr and Sr isotopic data, which reveal a conspicuously tight cluster of calcite-biotite and calcite-muscovite-based apparent ages around 30 Ma (27.3 to 33.4 Ma; Figure 15). Studies of the correlation between deformation textures and Sr-isotopic signatures show that synkinematic recrystallization of coexisting minerals in a deforming rock is usually accompanied by isotopic re-equilibration (Müller et al., 1999; Müller et al., 2000; Cliff and Meffan-Main, 2003; Glodny et al., 2008a). Sr-isotopic re-equilibration between minerals is equivalent to a complete reset of the Rb-Sr geochronological system. Most of the dated samples show clear indications for ductile deformation, like foliation-defining preferred orientation of mica. This is particularly true for sample T13-3, which is from a fine-grained, strongly sheared impure marble domain at the contact between a marble and a gneiss body (Figure 3a) and resembles part of a mylonite. In this sample, white mica-calcite pairs point to an age near 30 Ma, which therefore can be interpreted as the deformation age. For a synkinematic reset of the Rb-Sr system in white mica, temperatures of

at least 350 °C are required (Müller et al., 1999; Müller et al., 2000). With incomplete dynamic recrystallization or at static conditions, temperatures required to reset the Rb-Sr system of muscovitic white mica are much higher (near 600 °C, Glodny et al., 2008b). In consequence, the age cluster around 30 Ma is best explained as dating the waning stages of ductile deformation in both, the Bayindir and Selimiye nappes at temperatures near or in excess of 350 °C. In such a scenario, the higher apparent ages for biotite in sample 7-3740 (41 Ma; Figure 15) and the consistently higher but incoherent apparent ages for calcite-white mica pairs in all investigated samples except T13-3 (between ~36 and ~170 Ma; Figure 15) would reflect incompletely reset age signatures from previous metamorphic events, with no direct geological significance. As mentioned above, metamorphic temperatures at ~30 Ma were at least near 350 °C, and potentially considerably higher, as indicated by the stability of muscovite ± biotite ± epidote ± garnet in the silicate sub assemblage. Therefore, the 30 Ma ductile deformation event occurred contemporaneously in both nappes, at mid-crustal temperatures and at considerable depth. We infer that this 30 Ma event most likely dates the late stages of nappe stacking within a compressional tectonic regime. Incipient formation of the graben structure, therefore, must post-date this deformation and is inferred to be Late Oligocene to Miocene in age.

The above scenario is well in line with pre-existing geochronological data and interpretations. Ring et al.

(2003) proposed, based on $^{40}Ar/^{39}Ar$ muscovite ages and fission track ages for zircon and apatite, incipient extension-related cooling from the Late Oligocene onwards. An end of ductile deformation within the nappe stack roughly near 30 Ma is also in line with the presence of post-tectonic auriferous veins, formed at temperatures near 350 to 360 °C, and dated by in-situ analysis of K-feldspar and muscovite at 31.3 +/– 4.7 Ma (Şengün et al., 2019). Regionally, youngest biotite and muscovite ages near 30 Ma were also reported elsewhere (Hetzel and Reischmann, 1996; Satır and Friedrichsen, 1986). Older Rb/Sr and Ar/Ar mica apparent ages (> ~ 35 Ma), as detected here for Rb-Sr in muscovitic white mica and as reported from elsewhere in gneissic rocks and schists of the Menderes Massif (Hetzel and Reischmann, 1996; Satır and Friedrichsen, 1986; Koralay et al., 2015), may reflect earlier cessation of deformation in rocks of higher shear strength compared to the impure marbles of the present study. They may also be mixed ages with partial inheritance from earlier metamorphic stages as hypothesized for most of the here studied muscovite fractions.

Analysis of different samples of pure marble was undertaken to potentially constrain the deposition age of the marbles by means of Sr isotope stratigraphy (cf. McArthur et al., 2001). The observed variability of initial Sr isotopic ratios (between 0.7083 and 0.7123 for pure marbles, and between 0.7077 and 0.7153 for calcite from impure marbles, Supplementary Material 7) precludes a clear distinction between different marble units, as well as direct dating of depositional ages. Furthermore, the majority of the initial Sr isotopic ratios are higher than $^{87}Sr/^{86}Sr$ of Paleozoic or Mesozoic seawater (cf. McArthur et al., 2001). Therefore, marbles either were formed in non-oceanic basins or, more likely, there was a significant metasomatic overprint of the marbles with synmetamorphic exchange of Sr between the marine carbonate rocks and nearby silicate-rich rocks with their potentially much more radiogenic $^{87}Sr/^{86}Sr$ signatures.

The $^{87}Sr/^{86}Sr$ isotopic composition of four of the samples of pure marbles from surface outcrops do not show a consistent cluster but show rather variable values between 0.7083 and 0.7123 (Supplementary Material 7). A similar variability is seen in the initial Sr isotopic composition for the samples characterized by Rb-Sr geochronology. Here, the initial Sr isotopic composition (as approximated by the Sr isotopic composition of the low-Rb/Sr phase calcite) is between 0.7077 (sample 4-1325) and 0.7153 (sample 5-3655) (Figure 15; Supplementary Material 7). The majority of these initial Sr isotopic ratios are considerably higher than the $^{87}Sr/^{86}Sr$ ratio of seawater in Paleozoic to Mesozoic times (cf. McArthur et al., 2001).

To enhance the development of geothermal energy, detailed studies on the reservoir rocks are important. By the stratigraphic correlation of the GP-1 marble horizons, an improvement of the structural model was achieved. For future exploration drillings, the presence of the deeper, and because of the presumably higher temperature, more promising marble reservoir horizon was confirmed. Therefore, when investigating surface analogues and cuttings of an exploration well, a multiproxy approach is supportive by enhancing the geological model of the area for the determination of future well target zones. This leads to synergies and cost-effective development of new geothermal projects.

7. Conclusion

Two different marble horizons were drilled by the GP-1 geothermal exploration well near Koçarli (Büyük Menderes Graben, Turkey). Cuttings and stratigraphically well-defined surface samples allow correlation of cuttings to regional stratigraphic units by detailed comparison of their petrographical, geochemical and isotope properties. Several independent methods (macroscopic and microscopic petrography, major, trace and REY geochemistry, C, O and Sr stable isotopic composition, Rb-Sr geochronology) were combined in order to establish a geological model for the GP-1 well in the BMG.

The marble horizon at the bottom of GP-1 relates to the Cretaceous Bayındır nappe. In contrast, the shallow marble intersection is related to the Paleozoic Selimiye nappe. By this stratigraphic correlation, we were able to prove the nappe geometry of the BMG below the younger cover in the graben (from bottom to top: Bayındır, Bozdağ, Çine, and Selimiye). Ductile deformation in both the Bayındır and Selimiye nappes at upper-crustal temperatures and considerable depth is estimated at 30 Ma. The extensional graben structure must have formed < 30 Ma. Both, stable (C, O and Sr) and radiogenic (Rb-Sr) isotope data are modified by hydrothermal alteration.

We securely identified a second deeper reservoir in the graben with the Cretaceous marble, which promises higher reservoir temperatures (unpublished temperature logs by Borusan EnBW Enerji) and, therefore, a potentially higher economic efficiency for geothermal energy projects. Reservoir-specific characteristics can now be easily studied in representative surface analogues. The existence of two separate marble-dominated units at different depths in the Aydın-Koçarlı area has, thus, an important impact on future exploration and drilling campaigns as well as upscaling of existing geothermal sites in the vicinity. Accepting a lower reservoir temperature accompanied by reasonable drilling cost may lead to target the shallow marble reservoir. On the other hand, accepting higher total drilling cost, the deeper marble reservoir with higher temperature may become the focus of future project developers.

Authorship contributions

Conflicts of interest

Acknowledgment

References

Aksoy N (2014). Power generation from geothermal resources in Turkey. Renewable energy 68:595-601. doi: 10.1016/j.renene.2014.02.049

Bau M, Dulski P (1996). Distribution of yttrium and rare-earth elements in the Penge and Kuruman iron-formations, Transvaal Supergroup, South Africa. Precambrian Research 79: 37-55. doi: 10.1016/0301-9268(95)00087-9

Bau M, Möller P, Dulski P (1997). Yttrium and lanthanides in eastern Mediterranean seawater and their fractionation during redox-cycling. Marine Chemistry 56: 123-131. doi: 10.1016/S0304-4203(96)00091-6

Bozkurt E (2000). Timing of Extension on the Büyük Menderes Graben, Western Turkey, and Its Tectonic Implications. Journal of the Geological Society, London, Special Publications 173: 385-403. doi: 10.1144/GSL.SP.2000.173.01.18

Bozkurt E (2007). Extensional v. contractional origin for the southern Menderes shear zone, SW Turkey: tectonic and metamorphic implications. Geological Magazine 144: 191-210. doi: 10.1017/S0016756806002664

Bozkurt E, Oberhänsli R (2001). Menderes Massif (Western Turkey). Structural, metamorphic and magmatic evolution - a synthesis. International Journal of Earth Sciences 89: 679-708. doi: 10.1007/s005310000173

Bozkurt E, Park LRG (1994). Southern Menderes Massif: an incipient metamorphic core complex in western Anatolia, Turkey. Journal of the Geological Society, London 151: 213-216. doi: 10.1144/gsjgs.151.2.0213

Candan O, Dora OO, Oberhänsli R, Eikaplan M, Partzsch JH et al. (2001). Pan-African high-pressure metamorphism in the basement of the Menderes Massif, western Anatolia, Turkey. International Journal of Earth Sciences 89: 793-811. doi: 10.1007/s005310000097

Candan O, Dora OO, Oberhänsli R, Koralay E, Çetinkaplan M et al. (2011). Stratigraphy of the Pan-African basement of the Menderes Massif and the relationship with late Neoproterozoic/Cambrian evolution of the Gondwana. Bulletin of the Mineral Research and Exploration 142: 25-68.

Cliff RA, Meffan-Main S (2003). Evidence from Rb–Sr microsampling geochronology for the timing of Alpine deformation in the Sonnblick Dome, SE Tauern Window, Austria. In: Vance D, Müller W and Villa IM (eds) Geochronology: Linking the Isotopic Record with Petrology and Textures. Journal of the Geological Society, London, Special Publications 220: 159–172. doi: 10.1144/GSL.SP.2003.220.01.09

Condie KC (1993). Chemical composition and evolution of the upper continental crust: Contrasting results from surface samples and shales. Chemical Geology 104:1-37. doi: 10.1016/0009-2541(93)90140-E

Craig H, Craig V (1972). Greek marbles: determination of provenance by isotopic analysis. Science 176: 401-403. doi: 10.1126/science.176.4033.401

Cramer T (2004). Multivariate Herkunftsanalyse von Marmor auf petrographischer und geochemischer Basis. Das Beispiel kleinasiatischer archaischer, hellenistischer und römischer Marmorobjekte der Berliner Antikensammlung und ihre Zuordnung zu mediterranen und anatolischen Marmorlagerstätten. PhD, Technical University of Berlin (in German).

Dixon JE, Robertson AHF (1984). The Geological Evolution of the Eastern Mediterranean. Blackwell Scientific, London

Dora OO, Candan O, Kaya O, Koralay E, Dürr S (2001). Revision of "Leptite- gneisses" in Menderes Massif: a supracrustal meta-sedimentary origin. International Journal of Earth Sciences 89: 836-51. doi: 10.1007/s005310000102

Dürr S, Altherr R, Keller J, Okrusch M, Seidel E (1978). The median Aegean crystalline Belt: Stratigraphy, structure, metamorphism and magmatism. In: Cloos H, Roeder D, Schmidt K. (eds) Alps, Apennines, Hellenides. Schweizerbart'sche Verlag, Stuttgart, pp 455-477

Erdoğan B, Güngör T (2004). The problem of the core-cover boundary of the Menderes Massif and an emplacement mechanism for regionally extensive gneissic granites, Western Anatolia (Turkey). Turkish Journal of Earth Sciences 13: 15-36

General Directorate of Mineral Research and Exploration (MTA) (2015). Geoscience Map Viewer and Drawing Editor. http://yerbilimleri.mta.gov.tr/anasayfa.aspx. Accessed 12 March 2021

Germann K, Holzmann G, Winkler FJ (1980). Determination of marble provenance: Limits of isotopic analyses. Archaeometry 22: 99-106

Gessner K, Gallardo LA, Markwitz V, Ring U, Thomson SN (2013). What caused the denudation of the Menderes Massif. Review of crustal evolution, lithosphere structure, and dynamic topography in southwest Turkey. Gondwana Research 24:243-274. doi: 10.1016/j.gr.2013.01.005

Gessner K, Piazolo S, Güngör T, Ring U, Kröner A, Passchier CW (2001a). Tectonic significance of deformation patterns in granitoid rocks of the Menderes nappes, Anatolide belt, southwest Turkey. International Journal of Earth Sciences 89: 766-780. doi: 10.1007/s005310000106

Gessner K, Ring U, Lackmann W, Passchier CW, Güngör T et al. (1998). Structure and crustal thickening of the Menderes Massif, southwest Turkey, and consequences for large-scale correlations between Greece and Turkey. Bulletin of the Geological Society of Greece 32: 145-152

Gessner K, Ring U, Passchier CW, Güngör T (2001b). How to resist subduction: evidence for large-scale out-of-sequence thrusting during Eocene collision in western Turkey. Journal of the Geological Society, London 158: 769-784. doi: 10.1144/jgs.158.5.769

Gessner K, Ring U, Passchier CW, Hetzel R (2002). Discussion on „Stratigraphic and metamorphic inversions in the central Menderes Massif: a new structural model", by Aral I. Okay. International Journal of Earth Sciences 91:168-172. doi: 10.1007/s005310100223

Glodny J, Ring U, Kühn A (2008a). Coeval high-pressure metamorphism, thrusting, strike-slip, and extensional shearing in the Tauern Window, Eastern Alps. Tectonics 27 (4). doi: 10.1029/2007TC002193

Glodny J, Kühn A, Austrheim H (2008b). Geochronology of fluid-induced eclogite and amphibolite facies metamorphic reactions in a subduction–collision system, Bergen Arcs, Norway. Contributions to Mineralogy and Petrology 156 (1): 27-48. doi: 10.1007/s00410-007-0272-y

Gorgoni C, Lazzarini L, Pallante P, Turi B (1998). An updated and detailed mineropetrographic and C-O stable isotopic reference database for the main Mediterranean marbles used in antiquity. In: Herrmann J, Herz N, Newman R (editors): ASMOSIA 5. Interdisciplinary Studies on Ancient Stone - Proceedings of the Fifth International Conference of the Association for the Study of Marble and Other Stones in Antiquity, London

Gürer ÖF, Sarica-Filoreau N, Özburan M, Sangu E, Dogan B (2009). Progressive development of the Büyük Menderes Graben based on new data, western Turkey. Geological Magazine 146: 652-673. doi: 10.1017/S0016756809006359

Herz N (1987). Carbon and oxygen isotopic ratios: A data base for classical Greek and Roman marble. Archaeometry 29: 35-43. doi: 10.1111/j.1475-4754.1987.tb00395

Herz N, Dean NE (1986). Stable isotopes and archaeological geology: the Carrara marble, northern Italy. Applied Geochemistry 1: 139-151. doi: 10.1016/0883-2927(86)90045-4

Hetzel R, Reischmann T (1996). Intrusion age of Pan-African augen gneisses in the southern Menderes Massif and the age of cooling after Alpine ductile extensional metamorphism. Geological Magazine 133: 505-572. doi: 10.1017/S0016756800007846

Hoefs J (2015). Stable Isotope Geochemistry. Springer International Publishing, Cham

Hua G, Yuansheng D, Lian Z, Jianghai Y, Hu H (2013). Trace and rare earth elemental geochemistry of carbonate succession in the Middle Gaoyuzhuang Formation, Pinqguan Section: Implications for Early Mesoproterozoic ocean redox conditions. Journal of Palaeogeography 2 (2): 209-221. doi: 10.3724/SP.J.1261.2013.00027

Karamanderesi IH (2013). Characteristics of Geothermal Reservoirs in Turkey. In: International Geothermal Association Academy (ed): Geothermal Exploration.

Kaya A (2015). The effects of extensional structures on the heat transport mechanism: An example from the Ortakçi geothermal field (Büyük Menderes Graben, SW Turkey). Journal of African Earth Sciences (108): 74-88. doi: 10.1016/j.jafrearsci.2015.05.002

Kim ST, O'Neil JR (1997). Equilibrium and nonequilibrium oxygen isotope effects in synthetic carbonates. Geochimica et Cosmochimica Acta 61 (16): 3416-3475. doi: 10.1016/S0016-7037(97)00169-5

Koralay OE, Dora OO, Chen F, Satır M, Candan O (2004). Geochemistry and Geochonology of Orthogneisses in the Derbent (Alaşehir) Area, Eastern part of the Ödemiş-Kiraz Submassif, Menderes Massif: Pan-African Magmatic Activity. Turkish Journal of Earth Sciences 13: 37-61.

Koralay OE (2015). Late Neoproterozoic granulite facies metamorphism in the Menderes Massif, Western Anatolia/Turkey:implicationfortheassemblyofGondwana.Geodinamica Acta 27: 244-266. doi: 10.1080/09853111.2015.1014987

Lawrence MG, Greig A, Collerson KD, Kamber BS (2006). Rare Earth Element and Yttrium Variability in South East Queensland Waterways. Aquatic Geochemistry 12: 39-72. doi: 10.1007/s10498-005-4471-8

Lips ALW, Cassard D, Sözbilir H, Yilmaz H, Wijbrans JR (2001). Multistage exhumation of the Menderes Massif, western Anatolia (Turkey). International Journal of Earth Sciences 89: 781-792. doi: 10.1007/s005310000101

Loos S, Reischmann T (1999). The evolution of the southern Menderes Massif in SW Turkey as revealed by zircon dating. Journal of the Geological Society, London 156: 1021-1030. doi: 10.1144/gsjgs.156.5.1021

Ludwig KR (2003). User's manual for isoplot 3.00, a geochronlogical toolkit for Microsoft excel. Berkeley Geochronology Center, Special Publications 4: 25-32.

Manfra L, Masi U, Turi B (1975). Carbon and oxygen isotope ratios of marbles from some ancient quarries of western Anatolia and their archaeological significance. Archaeometry 17: 215-221. doi: 10.1111/j.1475-4754.1975.tb00135.x

McArthur JM, Howarth RJ, Bailey TR (2001). Strontium isotope stratigraphy: LOWESS version 3: best fit to the marine Sr-isotope curve for 0–509 Ma and accompanying look-up table for deriving numerical age. Journal of Geology, 109 (2): 155-170. doi: 10.1086/319243

McCrea JM (1950). On the Isotopic Chemistry of Carbonates and a Paleotemperature Scale. Journal of Chemical Physics 18: 849-857. doi: 10.1063/1.1747785

Meyer EE, Quicksall AN, Landis JD, Link PK, Bostick BC (2012). Trace and rare earth elemental investigation of a Sturtian cap carbonate, Pocatello, Idaho: evidence for ocean redox conditions before and during carbonate deposition. Precambrian Research 192-195: 89-106. doi: 10.1016/j.precamres.2011.09.015

Murdock HE, Gibb D, Andre T, Sawin JL, Brown A et al. (2021). Renewables 2021 - Global status report (INIS-FR-21-0788), International Nuclear Information system (INIS) 52 (25), France.

Müller W, Dallmeyer RD, Neubauer F, Thöni M (1999). Deformation induced resetting of Rb/Sr and 40Ar/39Ar mineral systems in a low-grade, polymetamorphic terrane (Eastern Alps, Austria). Journal of the Geological Society, London 156: 261–278.

Müller W, Mancktelow N, Meier M (2000). Rb–Sr microchrons of synkinematic mica in mylonites; an example from the DAV Fault of the Eastern Alps. Earth and Planetary Science Letters 180: 385–397

Münzner H, Schneiderhöhn P (1953). Das Sehnenschnittverfahren. Heidelberger Beiträge zur Mineralogie und Petrographie 3: 456-471. doi: 10.1007/BF01129198 (in German)

Origlia F, Gliozzo E, Gandin A, Meccheri M, Spangenberg JE et al. (2012). Marbles and carbonate rocks from central Morocco: a petrographic, mineralogical and geochemical study. Environmental Earth Sciences 66: 209–222. doi: 10.1007/s12665-011-1224-4

Özer S, Sözbilir H (2003). Presence and tectonic significance of Cretaceous rudist species in the so-called Permo-Carboniferous Göktepe Formation, central Menderes metamorphic Massif, western Turkey. International Journal of Earth Sciences 92: 397-404. doi: 10.1007/s00531-003-0333-z

Pereira HA, Frescura LM, Brumelhaus de Menezes B, Duarte R, Villetti MA et al. (2019). A multivariate approach at the thermodynamic properties of rare earth elements. Thermochimica Acta 678: 178315. doi: 10.1016/j.tca.2019.178315

Piper DZ, Bau M (2013). Normalized rare earth elements in water, sediments, and wine: identifying sources and environmental redox conditions. American Journal of Analytical Chemistry 4 (10A): 69-83. doi: 10.4236/ajac.2013.410A1009

Régnier JL, Mezger JE, Passchier CW (2007). Metamorphism of Precambrian–Paleozoic schists of the Menderes core series and contact relationships with Proterozoic orthogneisses of the western Çine Massif, Anatolide belt, western Turkey. Geological Magazine 144 (1): 67-104. doi: 10.1017/S0016756806002640

Régnier JL, Ring U, Passchier CW, Gessner K, Güngör T (2003). Contrasting metamorphic evolution of meta-sedimentary rocks from the Çine and Selimiye nappes in the Anatolide belt, western Turkey. Journal of Metamorphic Geology 21: 699-721. doi: 10.1046/j.1525-1314.2003.00473.x

Reilinger R, McClusky S, Vernant P, Lawrence S, Ergintav S et al. (2006). GPS constraints on continental deformation in the Africa-Arabia-Eurasia continental collision zone and implications for the dynamics of plate interactions. Journal of Geophysical Research 111: 1-26. doi: 10.1016/j.epsl.2013.10.018

Ricca M, Belfiore CM, Ruffolo SA, Barca D, Buergo MA de et al. (2015). Multianalytical approach applied to the provenance study of marbles used as covering slabs in the archaeological submerged site of Baia (Naples, Italy): The case of the "Villa con ingresso a protiro". Applied Surface Science 357: 1369-1379. doi: 10.1016/j.apsusc.2015.10.002

Ring U, Gessner K, Güngor T, Paschier CW (1999). The Menderes Massif of western Turkey and the Cycladic Massif in the Aegean; do they really correlate? Journal of the Geological Society, London 156: 3-6. doi: 10.1144/gsjgs.156.1.0003

Ring U, Johnson C, Hetzel R, Gessner K (2003). Tectonic denudation of a Late Cretaceous Tertiary collisional belt. Regionally symmetric cooling patterns and their relation to extensional faults in the Anatolide belt of western Turkey. Geological Magazine 140: 421-441. doi: 10.1017/S0016756803007878

Ring U, Willner AP, Lackmann W (2001). Stacking of nappes with different pressure-temperature paths. An example from the Menderes nappes of western Turkey. American Journal of Science 301: 912-944. doi: 10.2475/ajs.301.10.912

Rimmelé G (2003). Structural and metamorphic evolution of the Lycian nappes and the Menderes Massif (Southwest Turkey): Geodynamic implications and correlations with the Aegean domain. PhD, University of Potsdam

Rimmelé G, Jolivet L, Oberhänsli R, Goffé B (2003). Deformation history of the high-pressure Lycian nappes and implications for tectonic evolution of SW Turkey. Tectonics 22: 1-21. doi: 10.1029/2001TC901041

Rollinson HR (1993). Using Geochemical Data: Evaluation, Presentation, Interpretation: Taylor & Francis Ltd, London.

Rosen O, Desmons J, Fettes D (2007). Metacarbonate and related rocks. In: Fettes D, Desmons J (editors) Metamorphic Rocks. A Classification and Glossary of Terms, recommendations of the International Union of Geological Sciences Subcommission on the Systematics of Metamorphic Rocks.

Satır M, Friedrichsen H (1986). The origin and evolution of the Menderes Massif, W-Turkey: A rubidium/strontium and oxygen isotope study. Geologische Rundschau 75: 703-714. doi: 10.1007/BF01820642

Schuiling RD (1962). On petrology, age and structure of the Menderes migmatite complex (SW-Turkey). Bulletin of Mineral Research and Exploration 58: 71-84.

Şengör AMC, Yılmaz Y (1981). Tethyan evolution of Turkey: a plate tectonic approach. Tectonophysics 75: 181-241. doi: 10.1016/0040-1951(81)90275-4

Şengün F, Bertrandsson Erlandsson V, Hogmalm J, Zack T (2019). In situ Rb-Sr dating of K-bearing minerals from the orogenic Akçaabat gold deposit in the Menderes Massif, Western Anatolia, Turkey. Journal of Asian Earth Sciences 185: 104048. doi: 10.1016/j.jseaes.2019.104048

Şimşek Ş (1985). Geothermal model of Denizli, Sarayköy-Buldan area. Geothermics 14: 393-417. doi: 10.1016/0375-6505(85)90078-1

Spry A (1969). Metamorphic Textures. Pergamon Press, Oxford.

Tostevin R, Shields GA, Tarbuck GM, He T, Clarkson MO et al. (2016). Effective use of cerium anomalies as a redox proxy in carbonate-dominated marine settings. Chemical Geology 438: 146-162. doi: 10.1016/j.chemgeo.2016.06.027

Valley JW (1986). Stable isotope geochemistry of metamorphic rocks. In: Valley JW, Taylor HP, O'Neil JR (eds) Stable Isotopes in high temperature geological processes (Rev. Mineral. 16). Mineralogical Society of America, Washington, pp 445-489

van Hinsbergen, DJJ, Kaymakci N, Spakman W, Torsvik TH (2010). Reconciling the geological history of western Turkey with plate circuits and mantle tomography. Earth and Planetary Science Letters 297: 674-686. doi: 10.1016/j.epsl.2010.07.024

Villa IM, De Bièvre P, Holden NE, Renne PR (2015). IUPAC-IUGS recommendation on the half life of 87Rb. Geochimica et Cosmochimica Acta 164: 382-385. doi: 10.1016/j.gca.2015.05.025

Webb GE, Kamber BS (2000). Rare earth elements in Holocene reefal microbialites: A new shallow seawater proxy. Geochimica et Cosmochimica Acta 64 (9): 1557-1565. doi: 10.1016/S0016-7037(99)00400-7

Supplementary Material 1. Comparison of the metamorphic rocks and the related nomenclature of the Menderes Massif (modified after Régnier et al. 2003; 2007).

Rock types	Age	Classification		Reference
		„core-cover-model "	„nappe-stacking model"	
phyllite quartzite marble (Iğdecik Formation)	Lower Cretaceous	cover	Bayındır	Ring et al. 1999, Gessner et al. 2001a, Özer and Sözbilir 2003, Şimşek 1985
meta-pelite calcareous schist meta-marl marble-quartzite intercalation	Devonian-Carboniferous; meta-pelite protolith ~549 Ma (Ring et al. 2001)	core, partly cover	Selimiye	Schuiling 1962, Cağlayan et al. 1980, Satır and Friedrichsen 1986, Hetzel and Reischmann 1996, Régnier et al. 2003, 2007
augengneiss (meta-)granite intercalated mica schist paragneiss (containing eclogitic enclaves)	intrusion age of gneiss-protolith ~560-540 Ma	core	Çine	Candan et al. 2001, Dora et al. 2001, Hetzel and Reischmann 1996, Loos and Reischmann 1999
meta-pelite and meta-psammite meta-granite amphibolite eclogite	amphibolite and eclogite precursor (Proterozoic)	core/cover facies	Bozdağ	Candan et al. 2001, Koralay et al. 2004

Supplementary Material 2. List of methods applied to the different samples.

	#	1	2	3	4	5	6	7	8	9	10	11	12	13	14	15	16	17
samples	name	T1	T3	T4	T5-1	T11	T13-1	T13-2	T13-3	T13-4	1-1050	2-1065	3-1290	4-1325	5-3655	6-3680	7-3740	8-3865
	category	Cretaceous	Cretaceous	Cretaceous	Cretaceous	Cretaceous	Paleozoic	Paleozoic	Paleozoic	Paleozoic	well[S]	well[S]	well[S]	well[S]	well[D]	well[D]	well[D]	well[D]
geochemistry	C & O isotopic signature	X	X	X	X	X	X	X	X	X	X	X	X	X	X	X	X	X
	ICP-OES	X	X	X		X	X		X	X	X	X	X	X	X	X	X	X
	ICP-MS	X	X	X		X	X		X	X	X	X	X	X	X	X	X	X
	SEM-EDX	X	X		X	X	X	X	X	X	X	X		X			X	X
	Rb-Sr geo-chronology								X			X		X	X	X		X
	Sr isotopic signature	X	X				X			X								
petrography	colouring with Alizarin-S	X	X		X						X	X	X	X				
	pattern (calcite/dolomite)	X	X	X	X	X	X	X	X	X	X	X	X	X	X	X	X	X
	light transmission	X	X	X	X	X	X	X	X	X	X	X	X	X	X	X	X	X
	pyrite-bearing	X	X	X	X	X	X	X	X	X	X	X	X	X	X	X	X	X
	shape-preferred orientation (calcite/dolomite)	X	X	X	X	X	X	X	X	X	X	X	X	X	X	X	X	X
	grain size distribution (calcite/dolomite)	X	X	X	X	X	X	X	X	X	X	X	X	X	X	X	X	X
	maximum grain size (calcite/dolomite)	X	X	X	X	X	X	X	X	X	X	X	X	X	X	X	X	X
	fractures,	X	X	X	X	X	X	X	X	X		X						
	fissures	X	X	X	X	X	X	X	X	X		X						
	karst	X	X	X	X	X	X	X	X	X		X						
	colour	X	X	X	X	X	X	X	X	X	X	X	X	X	X	X	X	X

Marble samples → Calcitic Marbles / Dolomitic Marbles → Petrographic and textural properties (e.g. maximum grain size [MGS]) → Geochemical properties: main, trace & C-O isotopic composition → Hypothesised geological formation
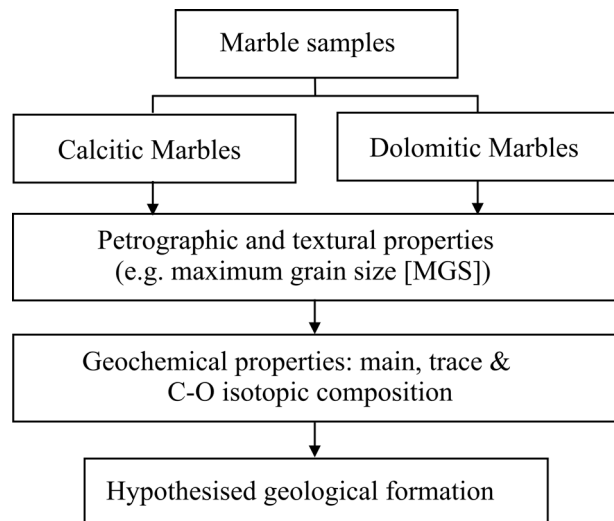
differentiate various marble types (originally provenance determination key, modified after Ricca et al., 2015).

Supplementary Material 4. Summary of petrographical observations. c: Cretaceous, p: Paleozoic.

	sample	origin	colour: white (w) or blueish light grey (bg)	calcitic (cc) or dolomitic (dol) marble; pure or impure (i)	maximum grain size [mm] (calcite/dolomite)	grain size distribution (calcite/dolomite) (eg: equally grained; ug: unequally grained)	shape-preferred orientation (calcite/dolomite)	pattern (calcite/dolomite)	pyrite-bearing	light transmission
1	T-1	c	w	cc, pure	1	eg	no	no	no	low
2	T-3	c	w	cc, pure	0.2	eg	no	no	no	very low
3	T-4	c	w	cc, i	3	eg	no	no	no	very low
4	T-5	c	w	cc, pure	1	ug	no	stained	no	very low
5	T-11	c	w	cc, pure	0.2	eg	no	no	no	very low
6	T13-1	p	bg	cc, pure	0.3	eg	elongated	striated	yes	medium
7	T13-2	p	bg	cc, pure	>10	ug	no	striated, partly mottled	yes	very low
8	T13-3	p	bg	dol, i	<0.2	eg	no	no	no	very low
9	T13-4	p	bg	cc, pure	0.3	eg	elongated	striated	yes	medium
10	1-1050	well[S]	bg	cc, i	0.3	eg	elongated	striated	no	low
11	2-1065	well[S]	bg	cc, i	0.3	eg	elongated	striated	no	medium
12	3-1290	well[S]	bg	cc, i	0.3	eg	elongated	striated	no	low
13	4-1325	well[S]	bg	cc, i	0.3	eg	elongated	striated	no	medium
14	5-3655	well[D]	w	cc, i	0.2	eg	no	few dark points	no	very low
15	6-3680	well[D]	w	cc, i	0.2	eg	no	no	no	very low
16	7-3740	well[D]	w	cc, i	0.2	eg	elongated	streaks	no	very low
17	8-3865	well[D]	w	cc, i	0.2	eg	no	no	no	very low

Supplementary Material 5. Results of major, trace and REE elements (ICP-MS/OES). c: Cretaceous; p: Paleozoic.

#		1	2	3	5	6	8	9	10	11	12	13	14	15	16	17
name		T1	T3	T4	T11	T13-1	T13-3	T13-4	1-1050	2-1065	3-1290	4-1325	5-3655	6-3680	7-3740	8-3865
category		c	c	c	c	p	p	p	well[s]	well[s]	well[s]	well[s]	well[D]	well[D]	well[D]	well[D]
oxides of major elements																
SiO_2	wt-%	n.a.	n.a.	n.a.	n.a.	n.a.	n.a.	n.a.	n.a.	n.a.	n.a.	n.a.	n.a.	n.a.	n.a.	n.a.
TiO_2	wt-%	n.a.	n.a.	n.a.	n.a.	n.a.	n.a.	n.a.	n.a.	n.a.	n.a.	n.a.	n.a.	n.a.	n.a.	n.a.
Al_2O_3	wt-%	0.043	0.017	0.221	0.440	0.036	0.871	0.035	0.718	0.325	2.782	3.160	12.104	7.644	13.073	17.231
$Fe_2O_{3\,tot}$	wt-%	0.126	0.073	1.340	0.283	0.090	0.743	0.067	0.870	0.374	1.665	1.753	3.190	2.036	2.569	1.389
MnO	wt-%	0.013	0.042	0.148	0.019	0.016	0.045	0.011	0.039	0.013	0.104	0.067	0.058	0.039	0.040	0.023
MgO	wt-%	1.520	0.402	6.201	0.555	2.949	18.943	1.184	2.500	0.979	0.904	1.084	2.063	1.013	0.936	0.362
CaO	wt-%	56.458	57.319	47.216	52.317	53.340	32.843	58.975	52.526	43.813	36.346	42.176	8.278	13.470	6.521	4.207
Na_2O	wt-%	0.007	<0.0027	<0.0027	<0.0027	0.020	<0.0027	<0.0027	<0.0027	<0.0027	0.061	0.129	3.233	1.619	3.079	3.603
K_2O	wt-%	<0.0024	<0.0024	<0.0024	<0.0024	<0.0024	<0.0024	<0.0024	<0.0024	<0.0024	0.008	0.029	1.239	0.979	2.520	4.776
P_2O_5	wt-%	0.0035	0.0050	0.0180	0.0030	0.0193	0.0505	0.0267	0.0150	0.0095	0.0133	0.0761	0.1662	0.0671	0.2007	0.1416
CO_2-calc	wt-%	45.968	45.422	43.826	41.664	45.081	46.459	47.576	43.953	35.454	29.511	34.283	8.749	11.677	6.140	3.697
totals	wt-%	104.138	103.280	98.970	95.281	101.551	99.955	107.876	100.621	80.967	71.394	82.759	39.081	38.544	35.078	35.429
trace elements																
Li	mg/kg	0.52	0.86	1.01	0.52	1.06	17.82	0.28	5.77	2.56	14.77	11.03	24.61	17.64	12.80	12.12
B	mg/kg	<0.43	<0.43	<0.43	<0.43	<0.43	<0.43	<0.43	0.84	2.03	<0.43	<0.43	<0.43	<0.43	<0.43	<0.43
P	mg/kg	15.22	21.83	78.68	13.11	84.17	220.26	116.62	65.30	41.64	58.15	332.08	725.31	292.80	875.71	617.96
Sc	mg/kg	0.27	0.35	0.30	0.68	0.11	0.79	0.14	1.35	0.82	3.71	5.05	6.96	4.76	5.54	3.39
V	mg/kg	3.29	0.58	2.60	4.07	1.32	13.04	1.48	5.30	3.02	20.87	34.93	56.23	35.04	38.43	21.46
Cr	mg/kg	2.02	0.87	1.72	13.54	0.57	9.05	0.98	4.52	1.93	15.56	38.39	44.58	29.00	25.87	9.70
Co	mg/kg	0.40	0.34	1.16	0.55	0.36	2.69	0.31	0.80	0.88	2.44	2.25	7.26	5.66	7.27	3.41
Ni	mg/kg	1.11	0.52	2.39	1.38	0.50	3.49	0.77	3.20	1.55	4.91	5.39	18.79	16.45	18.19	5.84
Cu	mg/kg	<0.03	<0.03	<0.03	<0.03	<0.03	<0.03	<0.03	0.51	0.88	2.75	31.83	45.42	8.84	11.88	10.69
Zn	mg/kg	<0.29	<0.29	<0.29	<0.29	<0.29	6.61	<0.29	4.51	11.19	5.39	12.73	35.46	22.27	21.51	40.03
As	mg/kg	1.72	0.35	0.39	0.97	0.29	1.19	0.76	1.16	0.42	0.43	1.01	0.99	0.54	0.67	1.15
Rb	mg/kg	0.282	0.111	1.647	3.947	<0.003	7.906	0.078	3.484	2.158	18.226	18.220	64.651	53.232	76.129	84.484
Sr	mg/kg	237.719	217.882	281.209	351.189	177.977	113.918	243.060	776.135	453.790	1808.443	2274.601	239.123	455.105	208.214	261.329
Y	mg/kg	3.641	7.707	8.405	4.198	1.982	3.937	2.680	9.833	6.291	13.988	13.567	17.939	11.426	20.421	13.644

Supplementary Material 5. (Continued).

Cd	mg/kg	0.199	0.234	0.178	0.271	0.132	0.150	0.159	0.583	0.353	0.065	0.050	0.092	0.066	0.035	0.204
Cs	mg/kg	0.021	0.021	0.156	0.303	0.046	0.281	0.034	0.181	0.135	0.714	0.602	3.865	1.708	2.268	1.444
Ba	mg/kg	4.41	17.79	55.63	13.37	7.29	57.02	5.68	26.34	10.00	36.76	31.84	1011.61	292.89	627.09	1844.69
Pb	mg/kg	1.60	0.65	3.15	2.75	0.58	0.97	0.85	3.48	1.71	6.74	4.77	8.50	7.61	13.34	42.36
Th	mg/kg	0.11	0.07	0.29	0.55	0.07	1.08	0.08	0.71	0.27	2.24	3.11	9.10	8.58	12.50	10.71
U	mg/kg	3.817	0.110	1.953	0.363	1.632	0.662	1.697	0.631	0.244	1.108	1.900	1.941	1.471	1.260	0.798
rare-earth elements																
La	mg/kg	1.45	4.58	2.67	2.01	0.72	2.76	1.05	5.44	2.71	9.51	17.01	22.88	16.48	27.50	25.82
Ce	mg/kg	1.26	4.86	5.69	3.37	0.86	4.14	1.36	7.15	2.55	18.25	30.99	48.01	33.40	58.55	53.05
Pr	mg/kg	0.270	0.898	1.020	0.484	0.148	0.650	0.220	1.157	0.534	2.313	3.763	5.853	4.103	7.062	6.050
Nd	mg/kg	1.099	3.891	4.696	1.930	0.592	2.624	0.875	4.758	2.175	9.357	14.632	22.711	15.762	27.071	22.527
Sm	mg/kg	0.215	1.042	1.073	0.417	0.119	0.517	0.163	0.971	0.446	2.034	2.724	4.576	2.946	5.409	4.313
Eu	mg/kg	0.052	0.620	0.310	0.103	0.032	0.104	0.039	0.238	0.110	0.486	0.567	0.993	0.639	0.975	1.441
Gd	mg/kg	0.277	1.231	1.214	0.482	0.167	0.549	0.221	1.147	0.552	2.218	2.629	4.465	2.738	5.082	4.065
Tb	mg/kg	0.046	0.186	0.179	0.080	0.027	0.084	0.035	0.184	0.089	0.369	0.401	0.664	0.391	0.747	0.565
Dy	mg/kg	0.297	0.944	0.988	0.451	0.182	0.488	0.229	1.142	0.583	2.264	2.290	3.471	2.098	3.877	2.819
Ho	mg/kg	0.071	0.170	0.189	0.095	0.047	0.102	0.056	0.253	0.136	0.464	0.466	0.641	0.395	0.749	0.499
Er	mg/kg	0.207	0.417	0.482	0.283	0.137	0.309	0.177	0.737	0.409	1.338	1.375	1.737	1.095	2.025	1.228
Tm	mg/kg	0.028	0.049	0.056	0.042	0.020	0.043	0.025	0.099	0.056	0.186	0.192	0.239	0.147	0.269	0.147
Yb	mg/kg	0.176	0.289	0.320	0.241	0.124	0.284	0.166	0.638	0.356	1.184	1.227	1.536	0.963	1.636	0.835
Lu	mg/kg	0.028	0.038	0.046	0.036	0.022	0.045	0.027	0.095	0.054	0.177	0.178	0.233	0.141	0.238	0.115
rare-earth elements ratios and anomalies																
Y/Ho	-	51.1	45.4	44.5	44.0	42.1	38.6	48.0	38.8	46.2	30.1	29.1	28.0	28.9	27.3	27.3
Ce/Ce*	-	0.55	0.68	0.74	0.80	0.68	0.74	0.71	0.73	0.56	0.92	0.93	0.92	0.90	0.92	0.94
Pr/Pr*	-	1.27	1.16	1.10	1.10	1.18	1.14	1.16	1.14	1.26	1.04	1.04	1.04	1.05	1.04	1.03
Eu/Eu*	-	0.99	2.54	1.27	1.07	1.05	0.91	0.93	1.05	1.02	1.07	1.00	1.03	1.06	0.87	1.62

Supplementary Material 6. Results of the $\delta^{13}C_{VPDB}$ and $\delta^{18}O_{VSMOW}$ stable isotope measurements.

#	name	origin	$\delta^{13}C_{VPDB}$	$\delta^{18}O_{VSMOW}$
surface samples			‰	‰
1	T1	Cretaceous	4.40	21.11
2	T3	Cretaceous	1.60	6.74
3	T4	Cretaceous	−0.42	13.45
4	T5-1	Cretaceous	−0.26	8.93
5	T11	Cretaceous	0.94	14.85
6	T13-1	Paleozoic	4.00	20.82
7	T13-2	Paleozoic	3.58	21.28
8	T13-3	Paleozoic	1.73	19.62
9	T13-4	Paleozoic	4.25	23.84
cutting samples				
10	1-1050	well[S]	1.76	18.17
11	2-1065	well[S]	2.11	18.52
12	3-1290	well[S]	2.16	18.85
13	4-1325	well[S]	3.00	20.07
14	5-3655	well[D]	−2.20	13.05
15	6-3680	well[D]	−2.83	13.74
16	7-3740	well[D]	−2.89	13.66
17	8-3865	well[D]	−1.57	15.28

Supplementary Material 7. Rb-Sr data. n.d.: not determined.

sample #	material	Rb in mg/kg	Sr in mg/kg	$^{87}Rb/^{86}Sr$	$^{87}Sr/^{86}Sr$	$^{87}Sr/^{86}Sr\ 2\sigma_m$
analysis						
T13-3						
PS3449	white mica > 250 μm	307	55.2	16.1	0.719112	0.0011
PS3450	white mica < 250 μm	323	12.6	74.4	0.744796	0.0014
PS3451	calcite	2.68	109	0.0709	0.712901	0.002
1-1050						
PS3460	white mica > 250 μm	351	155	6.54	0.715878	0.0016
PS3461	white mica < 250 μm	310	211	4.25	0.714283	0.0016
PS3462	calcite	0.87	616	0.0041	0.71022	0.0019
PS3463	biotite < 250 μm	490	21.7	65.5	0.738503	0.003
3-1290						
PS3456	biotite > 250 μm	436	93.1	13.6	0.714216	0.0022
PS3457	white mica > 250 μm	335	356	2.72	0.709947	0.0031
PS3458	white mica < 250 μm	321	400	2.32	0.709731	0.0028
PS3459	calcite	0.73	2369	0.00089	0.708584	0.0012
4-1325						
PS3464	biotite > 250 μm	416	42.2	28.5	0.720779	0.0021
PS3465	white mica < 250 μm	310	482	1.86	0.708938	0.0022
PS3466	white mica > 250 μm	341	407	2.43	0.709293	0.0018
PS3467	calcite	3.58	1592	0.00652	0.707675	0.0014
5-3655						
PS3445	biotite > 250 μm	260	14.3	53	0.736219	0.0022
PS3446	white mica > 250 μm	232	115	5.83	0.720568	0.0024
PS3447	white mica < 250 μm	209	120	5.06	0.719794	0.0016
PS3448	calcite	39.4	146	0.782	0.71533	0.0028
7-3740						
PS3452	biotite > 250 μm	346	27.8	36.1	0.730156	0.0024
PS3453	white mica > 250 μm	270	143	5.46	0.722326	0.002
PS3454	white mica < 250 μm	263	161	4.73	0.722	0.0021
PS3455	calcite	9.86	881	0.0324	0.709463	0.0013
Calcite from marble						
PS3468	calcite T1	n.d.	n.d.	n.d.	0.70838	0.0014
PS3469	calcite T3	n.d.	n.d.	n.d.	0.712295	0.0017
PS3470	calcite T13-1	n.d.	n.d.	n.d.	0.709222	0.0033
PS3471	calcite T13-4	n.d.	n.d.	n.d.	0.7093	0.0012

Supplementary Material 8. Characterization of samples by petrographical properties. The investigation on calcitic and dolomitic marble uses SEM-EDX measurements and petrographical description of hand specimens as well as thin sections and point counting of cuttings.

feature / sample	petrographical properties (macroscopic and microscopic)									
	Calcitic or dolomitic marble (○ calcitic, ● dolomitic, p pure, i impure)	colour (○ white, slightly grey, ● blueish light grey)	fractures, fissures (○ calcite fissures, ● hematite coated)	karst (× karst)	maximum grain size (calcite/dolomite) (○○○ fine (<2 mm), ●○○ medium (2–5 mm), ●●○ coarse (5–10 mm), ●●● very coarse (>10 mm))	grain size distribution (calcite/dolomite) (○ equally grained, ● unequally grained)	shape-preferred orientation (calcite/dolomite) (○ no orientation, ● elongated)	pyrite-bearing (○ no, ● yes)	light trans-mission (○○○ very low, ●○○ low, ●●○ medium, ●●● high)	pattern (calcite/dolomite) (○○○ none, ●○○ striated, ●●○ streaks, ●●● blotchy, ●●○ mottled, ○○○ dots)
surface samples										
# **name** **origin**										
1 T1 Cretaceous	○, p	○	●		○○○	○	○	○	●○○	○○○
2 T3 Cretaceous	○, p	○	●		○○○	○	○	○	○○○	○○○
3 T4 Cretaceous	○, i	○	●		●○○	○	○	○	○○○	○○○
4 T5-1 Cretaceous	○, p	○	○		○○○	●	○	○	○○○	●●●
5 T11 Cretaceous	○, p	○		×	○○○	○	○	○	○○○	○○○
6 T13-1 Paleozoic	○, p	●	●	×	○○○	○	●	●	●●○	●○○
7 T13-2 Paleozoic	○, p	●	●		●●●	●	○	●	○○○	●○○, ●○●
8 T13-3 Paleozoic	●, i	●	●		○○○	○	○	○	○○○	○○○
9 T13-4 Paleozoic	○, p	●	●	×	○○○	○	●	●	●●○	●○○
cutting samples										
10 1-1050 well[S]	○, i	●			○○○	○	●	○	●○○	●○○
11 2-1065 well[S]	○, i	●	○		○○○	○	●	○	●●○	●○○
12 3-1290 well[S]	○, i	●			○○○	○	●	○	●○○	●○○
13 4-1325 well[S]	○, i	●			○○○	○	●	○	●●○	●○○
14 5-3655 well[D]	○, i	○			○○○	○	○	○	○○○	○○○
15 6-3680 well[D]	○, i	○			○○○	○	○	○	○○○	○○○
16 7-3740 well[D]	○, i	○			○○○	○	●	○	○○○	●●○
17 8-3865 well[D]	○, i	○			○○○	○	○	○	○○○	○○○

Supplementary Material 9. Characterization of samples by geochemical properties. c: Cretaceous, p: Paleozoic.

feature / sample			Al₂O₃	Fe₂O₃ tot	MnO	MgO	CaO	Na₂O	K₂O	P₂O₅	δ¹³C VPDB	δ¹⁸O VSMOW	Sr	Y/Ho	Ce/Ce* (PAAS)	Pr/Pr* (PAAS)	Eu/Eu* (PAAS)
#	name	category															
surface samples																	
1	T1	c	○○○	○○○	○○○	●●○	●●●	○○○	×	○○○	●●●	●●●	●○○	●●○	●	●	●
2	T3	c	○○○	○○○	●●○	○○○	●●●	×	×	○○○	●○○	○○○	●○○	●●○	●	●	○
3	T4	c	●○○	●●○	●●●	●●●	●●○	×	×	●○○	●○○	○○○	●●○	●●○	●	●	●
4	T5-1	c									●○○	○○○					
5	T11	c	●○○	●○○	●○○	○○○	●●○	×	×	○○○	●○○	○○○	●●○	●●○	●	●	●
6	T13-1	p	○○○	○○○	○○○	●●○	●●○	●○○	×	●●○	●●●	●●○	○○○	●●○	●	●	●
7	T13-2	p									●●○	●●●					
8	T13-3	p	●●○	●○○	●●○	●●●	●●○	×	×	●●○	●●○	●●○	○○○	●○○	●	●	●
9	T13-4	p	○○○	○○○	○○○	●●○	●●●	×	×	●●○	●●●	●●●	●○○	●●○	●	●	●
cutting samples																	
10	1-1050	wellˢ	●●○	●○○	●●○	●●○	●●○	×	×	●○○	●●○	●○○	●●●	●○○	●	●	●
11	2-1065	wellˢ	●○○	●○○	○○○	●○○	●●○	×	×	○○○	●○○	●○○	●●●	●●○	●	●	●
12	3-1290	wellˢ	●●○	●●○	●●●	●○○	●●○	●○○	○○○	●○○	●●○	●○○	●●●	○○○	●	×	●
13	4-1325	wellˢ	●●○	●●●	●●●	●○○	●●○	●○○	●○○	●●●	●●○	●●○	●●●	○○○	●	×	●
14	5-3655	wellᴰ	●●●	●●●	●●●	●●○	●○○	●●●	●●○	●●●	○○○	●●○	●○○	○○○	●	×	●
15	6-3680	wellᴰ	●●●	●●●	●○○	●○○	●○○	●●○	●○○	●●○	○○○	○○○	●●●	○○○	●	×	●
16	7-3740	wellᴰ	●●●	●●●	●●○	●○○	●○○	●●○	●●○	●●●	○○○	○○○	○○○	○○○	●	×	●
17	8-3865	wellᴰ	●●●	●●○	●○○	○○○	●○○	●●●	●●●	●●●	○○○	○○○	●●○	○○○	●	×	○
			wt-%	wt-%	wt-%	wt-%	wt-%	wt-%	wt-%	wt-%	‰	‰	mg/kg	-	-	-	-
minimum value			0.017	0.067	0.011	0.362	4.207	0.007	0.008	0.003	-2.89	6.74	114	27.3	0.55	1.03	0.87
first quartile			0.132	0.205	0.017	0.920	23.157	0.050	0.267	0.011	-0.99	15.28	218	28.9	0.68	1.04	0.99
median			0.718	0.870	0.039	1.084	43.813	0.874	1.109	0.019	1.73	18.85	261	38.8	0.74	1.10	1.05
third quartile			5.402	1.709	0.052	2.282	52.933	3.117	2.200	0.072	3.29	20.44	455	45.4	0.92	1.16	1.07
maximum value			17.231	3.190	0.148	18.943	58.975	3.603	4.776	0.201	4.40	23.84	2275	51.1	0.94	1.27	2.54

element contents: × not present, ○○○ very low [< first quartile], ●○○ scarce / low [first quartile to < median], ●●○ abundant / medium [median to < third quartile], ●●● very abundant / high [≥ third quartile]; **isotopic values**: from low to high values; **Y/Ho ratio**: ○○○ < 33, ●○○ 33–40, ●●○ 40–80, ●●● > 80; **Ce/Ce*₍PAAS₎**: ● ≤ 0.95, ○ > 0.95; **Pr/Pr*₍PAAS₎**: ● oxic (> 1.05), ○ anoxic (< 0.95), × 0.95–1.05; **Eu/Eu*₍PAAS₎**: ● ≤ 1.5, ○ > 1.5
(geochemical values originally in wt.-%, δ-values in ‰)